Journal of Computational Physics 565 (2026) 115215

Contents lists available at ScienceDirect

Journal of Computational Physics

journal homepage: www.elsevier.com/locate/jcp

A comparative study of fine-scale and multi-scale finite-volume and finite-element methods for coupled poroelastic problems

Mahsa Mehrazar [a,*], Cornelis Vuik [a], Mohammed Al Kobaisi [b], Hadi Hajibeygi [c]

[a] Delft Institute of Applied Mathematics, Faculty of Electrical Engineering, Mathematics and Computer Science, Delft University of Technology, Delft, The Netherlands
[b] Department of Chemical and Petroleum Engineering, Khalifa University of Science and Technology, Abu Dhabi, United Arab Emirates
[c] Department of Geoscience and Engineering, Faculty of Civil Engineering and Geosciences, Delft University of Technology, Delft, The Netherlands

ARTICLE INFO

Keywords:
Multiscale method
Finite element method
Finite volume method
Porous media

ABSTRACT

Coupled geomechanical deformation and fluid flow phenomena arise in a wide range of subsurface processes, such as reservoir compaction, subsidence, and fault reactivation. Accurate and efficient simulation of these phenomena requires robust and consistent numerical formulations capable of capturing hydro-mechanical (HM) behavior in porous media. This study presents a detailed comparative numerical investigation of the multiscale finite-volume (MSFV) and multiscale finite-element (MSFE) formulations for fully coupled poroelastic problems. Both formulations are developed within a unified multiscale framework employing local basis functions, along with restriction and prolongation operators, to ensure consistent transfer of information between fine and coarse grids. The governing Biot equations, incorporating the balance of linear momentum and fluid mass, are solved in a fully implicit manner to achieve stable hydro-mechanical coupling. The MSFV formulation is based on a conservative staggered-grid discretization that guarantees local mass and stress conservation, whereas the MSFE approach utilizes continuous Galerkin (CG) interpolation providing smooth displacement and pressure fields. Performance, stability, and computational efficiency are assessed through benchmark problems, including Terzaghi's consolidation, Mandel's problem, and a heterogeneous permeability test. Our results indicate that both formulations accurately reproduce fine-scale reference solutions, while a hybrid discretization combining finite elements for displacement and finite volume for pressure delivers the most favorable balance between accuracy, stability, and conservation.

1. Introduction

Accurately simulating the coupled interaction between fluid flow and mechanical deformation in subsurface geological formations remains a significant challenge, since these problems typically involve large-scale models with highly heterogeneous material properties and strong hydro-mechanical (HM) coupling. Within the framework of Biot's poroelasticity theory [1], subsurface flow and mechanical deformation are intrinsically coupled via effective stress and mass accumulation, which together govern reciprocal interaction between hydraulic and mechanical responses. These poromechanical interactions are fundamental to a wide range of geoscientific and engineering applications, including geothermal energy extraction and underground storage of carbon dioxide and hydrogen. Accurate and scalable methods for numerical simulation of these coupled processes is therefore essential for reliable predictions [2].

* Corresponding author.
E-mail address: M.Mehrazar@tudelft.nl (M. Mehrazar).

https://doi.org/10.1016/j.jcp.2026.115215
Received 16 January 2026; Received in revised form 7 July 2026; Accepted 15 July 2026
Available online 18 July 2026

Achieving accurate predictions typically demands high-resolution models capable of representing fine-scale variations in permeability and elastic moduli, since these heterogeneities strongly influence the coupled fluid-solid response. Yet such detailed simulations become impractical in large-scale field applications, where computational cost grows rapidly with model complexity. This challenge motivates the development of advanced numerical strategies that represent the heterogeneous properties at fine scales while allowing for construction of coarse-scale systems to remain scalable for field applications.

In computational practice, finite-volume (FV) schemes are widely adopted for simulating flow and transport because of their local conservative properties and compatibility with reservoir simulation [3,4], whereas finite-element (FE) methods are typically preferred for mechanical deformation due to their flexibility in representing stress-strain behavior especially on complex grids [5]. Several hybrid and mixed formulations have been introduced and developed to combine the strengths of finite-volume and finite-element schemes for both flow and mechanical deformation [6,7]. Building on this line of work, problems involving sharp permeability contrasts or complex physics tend to benefit from using discontinuous pressure representations. Many geoscience applications, such as multiphase flow [8] and THM driven convection [9], also require strict element-wise mass conservation. Hence, these considerations have made FE-FV combinations a practical and widely used choice in reservoir modeling by pairing finite-elements for the mechanical response and finite volumes for fluid flow [10]. Alongside these developments, finite-difference schemes have been applied to Biot-type poromechanical systems [11], and more recent work has explored finite-volume discretization for mechanical deformation in both continuous and fractured media [12–14]. These FV-based schemes are often motivated by their ability to produce locally conservative discrete stress fields while relying on a single degree of freedom per element, which benefits large-scale simulations. Motivated by the necessity to account for mechanical effects even in problems where flow dominates, several studies have also explored face-centered and cell-centered FV formulations for the mechanical response [15–18]. These efforts have broadened the range of fully consistent FV-based hydro-mechanical approaches. Effective coupling of these two numerical frameworks is therefore central to large-scale poromechanical simulation, and the design of computationally efficient algorithms plays a decisive role in enabling predictive modeling at realistic field scales.

Depending on computational constraints and desired accuracy, this coupling may be enforced sequentially or via fully implicit formulations. Finite-volume formulations for poromechanics have also been implemented within sequential or loosely coupled flow-mechanics strategies [19], in which the two subproblems are solved separately. While such sequential schemes remain computationally attractive, especially for large-scale reservoir applications, they require careful handling of the coupling terms to maintain stability and accuracy. In contrast, fully implicit formulations [20] solve both fields simultaneously, which improves stability at the cost of higher computational complexity and avoids several errors that arise in sequential schemes.

Regardless of the employed discretization strategy and coupling approach, to address the computational challenges associated with fine-scale simulations, multiscale approaches have emerged as powerful tools that enable accurate coarse-scale representations while preserving essential fine-scale physics. Poromechanical response of subsurface formations depends strongly on the fine-scale structure of permeability and elastic properties. In real-field applications, however, fully resolving the geometry and property variations of subsurface media is rarely feasible. Multiscale (MS) formulations address this challenge by employing various upscaling and downscaling mechanisms to capture the interaction between fine and coarse scales. These mechanisms range from classical homogenization concepts [21,22] to localized numerical basis constructions, and a comprehensive review of multiscale techniques in porous media is provided in [23].

To address the computational challenges associated with fine-scale simulations, the multiscale finite-volume (MSFV) [24–27] and multiscale finite-element (MSFE) [28–32] approaches have been applied successfully to represent flow and deformation in heterogeneous porous media [33–37]. Multiscale methods have gradually evolved to accommodate increasingly complex physical processes. Early developments focused on static two-level formulations in sequential multiscale simulators, particularly for flow and transport problems with nonlinear and multiphase behaviors [38–40]. More recent work has introduced dynamic multilevel constructions suitable for fully implicit and strongly coupled systems [41–43]. Parallel to these advances, multiscale FE formulations have been extended to solid mechanics, using fine-scale FE operators to represent heterogeneous elastic behavior [44–47]. Moreover, recent studies further demonstrate that multiscale techniques can remain accurate and computationally robust even in highly heterogeneous media containing fractures [48,49]. Complementary to these multiscale approaches, the resulting large-scale linear systems are typically too expensive for sparse direct solvers, which makes fast converging iterative methods [50–54] essential. Much of the effort in this area has centered on developing effective preconditioned Krylov solvers [55–61] and multigrid techniques [62–64], particularly for the classical two-field ($u - p$) formulation that is widely used in consolidation modeling [65–67].

Building upon this foundation and the two-level multiscale methods based on local basis functions [46,68], this paper presents a comprehensive comparative study of MSFV, MSFE, and hybrid FE-FV strategies for coupled Poroelastic problems within a unified framework. Building on the complementary strengths of FV (local mass conservation) and FE (geometric flexibility), and on prior multiscale developments, we formulate a fully-implicit MSFV- and MSFE-based discretization for linear poroelasticity. Compared with the sequential approaches, the coupled formulation enhances numerical stability and generates a convenient framework for the cases with strong flow-deformation coupling terms. Local basis functions for both pore pressure and deformation vector are computed subject to local boundary conditions, used to assemble the coarse system, and then applied to reconstruct an approximated fine-scale solution. Through this comparison, we aim to clarify the benefits and limitations of MSFV versus MSFE in practical poroelastic simulations, with a focus on stability, conservation, and scalability.

The remainder of this paper is organized as follows. Section 2 introduces Biot's governing equations for poroelasticity and presents the FV and FE discretization frameworks, followed by a brief derivation of the multiscale formulation. Section 3 reports numerical results on benchmarks, including the one-dimensional Terzaghi consolidation and the two-dimensional Mandel problem, and further

examines an elliptic pressure equation on a heterogeneous domain with a mobility field of varying orientation angles, each compared against the fine-grid solution. Finally, some concluding remarks are outlined in Section 4.

2. Governing equations

2.1. Strong form

In order to model the single-phase flow of slightly compressible fluid through a saturated deformable porous medium, the coupled governing equations are presented based on the linear momentum and mass conservation within the framework of Biot's poroelasticity theory. Let the problem domain be denoted by $\Omega \subset \mathrm{R}^2$ over the time interval $\mathcal{T} = (0, T]$, with boundary $\partial\Omega = \Gamma$. The porous medium is considered fully saturated, and the solid matrix is assumed to behave as a linear elastic material. The momentum balance of the mixture is given by

$$\nabla \cdot \boldsymbol{\sigma} + \mathbf{f} = \nabla \cdot \left(\boldsymbol{\sigma}' - \alpha p \mathbf{I}\right) + \mathbf{f} = 0, \tag{1}$$

where $\nabla\cdot$ is the divergence operator and ∇ the gradient operator, $\boldsymbol{\sigma}$ is the total stress, $\mathbf{f}$ represents the body forces, $\boldsymbol{\sigma}'$ denotes the effective Cauchy stress, α is the Biot coefficient, $\mathbf{I}$ is the identity matrix, and p represents the pore pressure. The effective Cauchy stress is defined as $\boldsymbol{\sigma}' = \mathbf{C} : \boldsymbol{\varepsilon}$, in which $\mathbf{C}$ denotes the drained elasticity tensor, and $\boldsymbol{\varepsilon}$ represents the strain tensor. In all simulations presented in this study, the body force term is assumed to be zero. For an isotropic material, the drained elasticity matrix is defined in terms of the Lamé parameters of λ and μ as

$$\mathbf{C} = \begin{bmatrix} \lambda + 2\mu & \lambda & 0 \\ \lambda & \lambda + 2\mu & 0 \\ 0 & 0 & \mu \end{bmatrix}, \tag{2}$$

where $\lambda = \dfrac{E\nu}{(1+\nu)(1-2\nu)}$ and $\mu = \dfrac{E}{2(1+\nu)}$ with E and ν representing Young's modulus and Poisson's ratio, respectively. Within the small strain framework, the compatibility equation is written as

$$\boldsymbol{\varepsilon}(\mathbf{u}) = \nabla^s \mathbf{u} = \frac{1}{2}\left(\boldsymbol{\nabla}\mathbf{u} + (\boldsymbol{\nabla}\mathbf{u})^T\right). \tag{3}$$

The quantities $\mathbf{u}$ and $\nabla^s\mathbf{u}$ denote the displacement vector and its symmetric gradient, respectively. The volumetric strain then reads

$$\varepsilon_v = \mathrm{tr}(\boldsymbol{\varepsilon}) = \nabla \cdot \mathbf{u}. \tag{4}$$

The mass balance of the fluid phase is expressed as

$$\alpha \frac{\partial \varepsilon_v}{\partial t} + \frac{1}{Q}\frac{\partial p}{\partial t} + \boldsymbol{\nabla} \cdot \mathbf{w} = q \tag{5}$$

in which Q, $\mathbf{w}$ and q are the Biot modulus, the Darcy velocity vector of the fluid with respect to the solid skeleton, and the volumetric source or sink term, respectively. In addition, the fluid relative velocity vector is described by Darcy's law as

$$\mathbf{w} = -\boldsymbol{\Lambda}\boldsymbol{\nabla} p, \tag{6}$$

where $\boldsymbol{\Lambda} = \frac{\mathbf{k}}{\mu}$ denotes the mobility tensor expressed in terms of the rock permeability tensor $\mathbf{k}$ and the fluid viscosity μ. The primary unknown variables are the displacement $\mathbf{u}$ and the pore pressure p, which define the standard $\mathbf{u} - p$ formulation. Moreover, $\dot{\varepsilon_v} = \frac{\partial \varepsilon_v}{\partial t}$ and $\dot{p} = \frac{\partial p}{\partial t}$ represent the time derivatives of the corresponding variables. The above equations, together with appropriate boundary and initial conditions, form a well-posed coupled hydro-mechanical (HM) problem. As depicted in Fig. 1, the boundary Γ is decomposed into regions where Dirichlet and Neumann boundary conditions are specified, denoted by $\Gamma = \Gamma_u^D \cup \Gamma_u^N$ for momentum balance and $\Gamma = \Gamma_p^D \cup \Gamma_p^N$ for the mass balance. These divisions follow the overlap restriction $\Gamma_u^D \cap \Gamma_u^N = \Gamma_P^D \cap \Gamma_u^N = \emptyset$. The conditions can be stated as

$$\begin{aligned}
\mathbf{u} &= \bar{\mathbf{u}} && \text{on } \Gamma_u^D \times \mathcal{T}, \\
\boldsymbol{\sigma} \cdot \mathbf{n} &= \bar{t} && \text{on } \Gamma_u^N \times \mathcal{T}, \\
p &= \bar{p} && \text{on } \Gamma_p^D \times \mathcal{T}, \\
\mathbf{w} \cdot \mathbf{n} &= \bar{q} && \text{on } \Gamma_p^N \times \mathcal{T}, \\
\mathbf{u}(\boldsymbol{x}, 0) &= \mathbf{u}_0(\boldsymbol{x}) && \text{on } (\boldsymbol{x}, t) \in \Omega \times \{0\}, \\
p(\boldsymbol{x}, 0) &= p_0(\boldsymbol{x}) && \text{on } (\boldsymbol{x}, t) \in \Omega \times \{0\}.
\end{aligned} \tag{7}$$

Here, $\mathbf{n}$ denotes the outward normal vector, and the overbars represent prescribed boundary values. The quantities $\bar{\mathbf{u}}$ and $\bar{p}$ define Dirichlet boundary conditions associated with displacement and pore pressure on Γ_u^D and Γ_p^D, respectively. Similarly, $\bar{t}$ and $\bar{q}$ define Neumann boundary conditions corresponding to the applied mechanical traction and normal Darcy flux on Γ_u^N and Γ_p^N, respectively. A positive value of $\bar{q}$ indicates production, whereas a negative value represents injection.

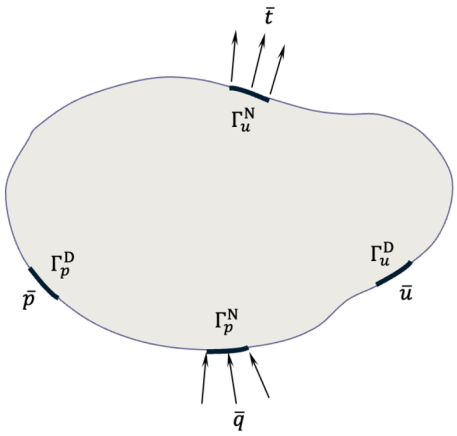

Fig. 1. Schematic illustration of the boundary conditions imposed on the porous medium domain.

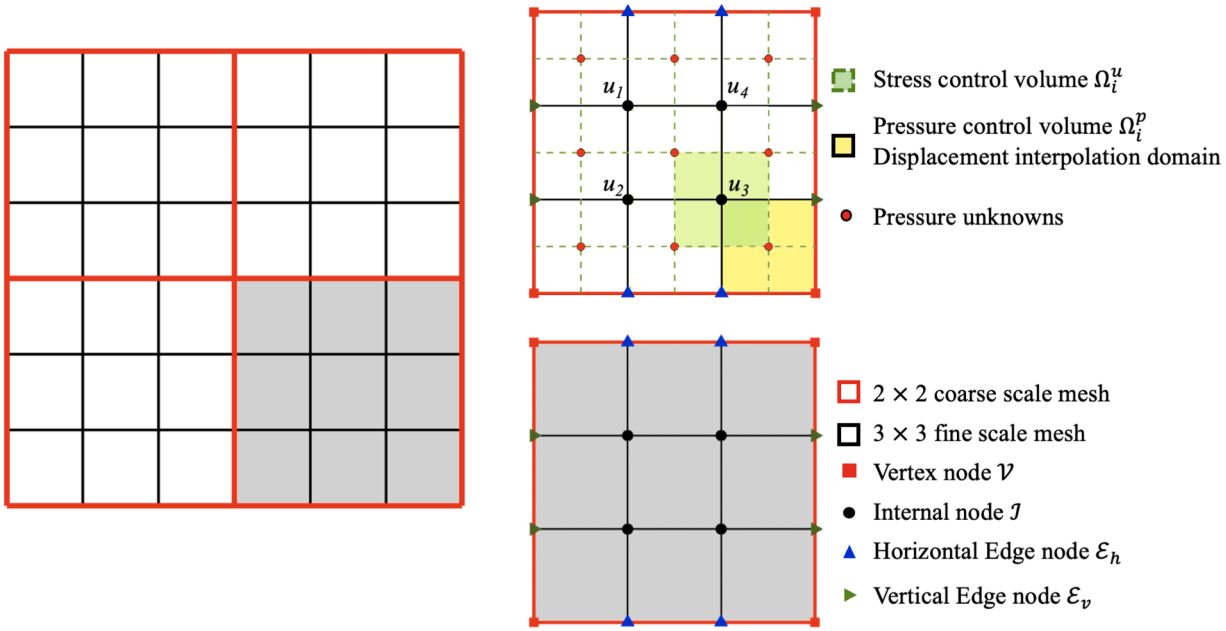

Fig. 2. Illustration of the coarse-scale and fine-scale staggered grids for pressure and displacement. Four node types are defined: vertex nodes ($\mathcal{V}$) located at the corners of the coarse cells, internal nodes ($\mathcal{I}$) residing within each coarse block, horizontal edge nodes ($\mathcal{E}_h$) positioned along the horizontal edges, and vertical edge nodes ($\mathcal{E}_v$) along the vertical edges.

2.2. Spatial discretization

This section outlines the finite-volume (FV) and finite-element (FE) weak formulations of the coupled Hydro-Mechanical (HM) system. Both methods solve the same governing equations but differ in their spatial discretization approaches and variable definitions.

2.2.1. Finite volume based formulation

The finite-volume (FV) formulation relies on a control-volume (CV) strategy in which displacement and pressure unknowns are defined on a staggered grid, where the pressure DOFs are located at the centers of the primal-mesh control volumes. As shown in Fig. 2, displacement DOFs are located at the vertices of a dual mesh, each associated with a stress control volume. This staggered arrangement ensures local conservation and provides a consistent data structure for the permeability and elastic parameters, which is particularly advantageous in heterogeneous formations.

Integrating the momentum balance equation over the stress control volumes Ω_i^u reads

$$\int_{\Omega_i^u} \nabla \cdot (\mathbf{C} : \nabla^s \mathbf{u} - \alpha p \mathbf{I})\, dV = -\int_{\Omega_i^u} \mathbf{f}\, dV, \tag{8}$$

which is then re-stated as

$$\int_{\partial\Omega_i^u} (\mathbf{C} : \nabla^s \mathbf{u} - \alpha p \mathbf{I}) \cdot \mathbf{n}\, dS = -\int_{\Omega_i^u} \mathbf{f}\, dV \tag{9}$$

using the divergence theorem. Here, the first term corresponds to the pure mechanical response, whereas the second term accounts for the coupling introduced by pore-pressure variations. Similarly, integrating the mass balance equation over the pressure control volumes Ω_j^p gives

$$\int_{\Omega_i^p} \alpha\, \nabla \cdot \dot{\mathbf{u}}\, dV + \int_{\Omega_i^p} \left(\frac{1}{Q} \dot{p} - \nabla \cdot (\mathbf{\Lambda} \nabla p) \right) dV = \int_{\Omega_i^p} q\, dV \tag{10}$$

which, after applying the divergence theorem, becomes

$$\int_{\partial\Omega_i^p} \alpha\, (\dot{\mathbf{u}} \cdot \mathbf{n}) dS + \frac{1}{Q} \int_{\Omega_i^p} \dot{p}\, dV - \int_{\partial\Omega_i^p} (\mathbf{\Lambda} \nabla p) \cdot \mathbf{n}\, dS = \int_{\Omega_i^p} q\, dV. \tag{11}$$

The first term on the left-hand side explicitly couples the fluid flow and the solid deformation, thereby reflecting the strong hydro-mechanical interaction. The continuous fields are approximated within each control volume as follows. The displacement field is interpolated over the nodes of each displacement control volume as

$$\mathbf{u}(x, y) \approx \mathbf{u}^h(x, y) = \sum_{i=1}^{4} \mathbf{u}_i\, N_i(x, y) \qquad \text{for } (x, y) \in \Omega_i^u, \tag{12}$$

where $\mathbf{u}_i$ denotes the nodal displacement and $N_i(x, y)$ are the bilinear shape functions corresponding to each node of the element Ω_i^u. This interpolation ensures smooth variation of displacements and strains across control-volume boundaries. Pressure, on the other hand, is assumed to be piecewise constant within each pressure control volume as

$$p(x, y) \approx p_i \qquad \text{for } (x, y) \in \Omega_i^p, \tag{13}$$

where p_i is the cell-centered value for the pressure field. This combination of bilinear interpolation for displacement and a classical constant interpolation for pressure provides a locally conservative stress field, while also reducing the number of degrees of freedom and, consequently, reducing the computational cost compared to mixed finite-element methods [14,37].

2.2.2. Finite element based formulation

The weak form of the momentum balance is first obtained by multiplying the strong form of equations by the virtual test function $\delta\mathbf{u}$ and then integrating over the whole domain Ω as follows

$$\int_{\Omega} \delta\mathbf{u} \cdot (\nabla \cdot (\mathbf{C} : \nabla^s \mathbf{u}) - \nabla \cdot (\alpha p \mathbf{I}))\, \mathrm{d}\Omega = -\int_{\Omega} \delta\mathbf{u}\ \mathbf{f}\ \mathrm{d}\Omega \tag{14}$$

Following a similar approach, the weak form of the mass balance for bulk is derived by multiplying Eq. (5) by its corresponding test function δp. The integration is then carried over Ω, which leads to

$$\int_{\Omega} \delta p \left(\alpha\, \nabla \cdot \dot{\mathbf{u}} + \frac{1}{Q} \dot{p} - \nabla \cdot (\mathbf{\Lambda} \nabla p) \right) \mathrm{d}\Omega = \int_{\Omega} \delta p\, q\, \mathrm{d}\Omega \tag{15}$$

By applying the divergence theorem and integration by parts to the integral Eqs. (14) and (15), their extended forms can be written as

$$\int_{\Omega} (\nabla^s \delta\mathbf{u}) : \mathbf{C} : \nabla^s \mathbf{u}\, \mathrm{d}\Omega\ -\ \int_{\Omega} \alpha p \nabla \cdot (\delta\mathbf{u})\ \mathrm{d}\Omega\ =\ \int_{\Gamma_u^N} (\delta\mathbf{u}) \cdot \bar{\boldsymbol{t}}\, \mathrm{d}\Gamma\ -\ \int_{\Omega} (\delta\mathbf{u})\, \mathbf{f}\, \mathrm{d}\Omega \tag{16}$$

$$\int_{\Omega} (\nabla \delta p) \cdot \mathbf{\Lambda} \cdot \nabla p\, \mathrm{d}\Omega\ +\ \alpha \int_{\Omega} \delta p\, \nabla \cdot \dot{\mathbf{u}}\, \mathrm{d}\Omega\ +\ \int_{\Omega} \delta p\, \frac{1}{Q} \dot{p}\, \mathrm{d}\Omega =\ -\ \int_{\Gamma_p^N} \delta p\, \bar{q}\, \mathrm{d}\Gamma\ +\ \int_{\Omega} \delta p\, q\, \mathrm{d}\Omega \tag{17}$$

Following the Continuous Galerkin (CG) framework, the displacement and pore pressure fields are approximated with bilinear and piecewise linear basis functions, respectively. Therefore, the exact solutions are approximated on fine-scale mesh resolution Ω^h, where super-index h denotes the fine-scale mesh, as

$$\mathbf{u} \approx \mathbf{u}^h(\boldsymbol{x}, t) = \mathbf{N}_{\mathrm{u}}(\boldsymbol{x})\, \hat{\mathbf{u}}(t) \tag{18}$$

and

$$p \approx p^h(\boldsymbol{x}, t) = \mathbf{N}_p(\boldsymbol{x})\, \hat{p}(t), \tag{19}$$

where $\hat{\mathbf{u}}(t)$ and $\hat{p}(t)$ are the displacement and pressure unknowns at the nodes, $\mathbf{N}_p(\boldsymbol{x})$ denotes the pressure shape function and $\mathbf{N}_u(\boldsymbol{x})$ is the matrix of the displacement shape functions. The corresponding gradients are also approximated as

$$\boldsymbol{\nabla}\mathbf{u}^h = \mathbf{B}\, \hat{\mathbf{u}}, \qquad \nabla p^h = \mathbf{G}\, \hat{p}. \tag{20}$$

Here, $\mathbf{B}$ and $\mathbf{G}$ are constructed from the gradients of the element shape functions $\boldsymbol{\nabla}\mathbf{N}(\boldsymbol{x})$, and $\hat{u}_i$ and $\hat{p}_i$ denote the nodal displacement and pressure unknowns, respectively. For quadrilateral elements, bilinear shape functions are employed, whereas for triangular

elements, linear interpolations are typically used. Substitution of the above approximations into the weak form leads to the residual-based discrete FE system, i.e.,

$$\begin{aligned}\boldsymbol{\psi}_u &= \mathbf{K}_{uu}\,\mathbf{U} - \mathbf{Q}_{up}\,\mathbf{P} - \mathbf{F}_u = \mathbf{0},\\ \boldsymbol{\psi}_p &= \mathbf{Q}_{pu}\,\dot{\mathbf{U}} + \mathbf{S}_{pp}\,\dot{\mathbf{P}} + \mathbf{R}_{pp}\,\mathbf{P} - \mathbf{F}_p = \mathbf{0}.\end{aligned} \tag{21}$$

Here, in the residual vectors of $\boldsymbol{\psi}_u$ and $\boldsymbol{\psi}_p$, $\mathbf{K}_{uu}$ is the stiffness matrix, $\mathbf{R}_{pp}$ is the hydraulic conductivity (transmissibility) matrix, $\mathbf{S}_{pp}$ is the storage (or compressibility, accumulation) matrix, and $\mathbf{Q}_{pu}$ is the flow-deformation coupling term. The vectors $\mathbf{F}_u$ and $\mathbf{F}_p$ include the mechanical forces and hydraulic fluxes, respectively. The corresponding element-level matrices and vectors are defined as

$$\begin{aligned}\mathbf{K}^e_{uu} &= \int_{\Omega^e} \mathbf{B}^{\mathrm{T}}\,\mathbf{C}\,\mathbf{B}\,\mathrm{d}\Omega,\\ \mathbf{Q}^e_{up} &= \mathbf{Q}^T_{pu} = \int_{\Omega^e} \mathbf{B}^{\mathrm{T}}\,\alpha\mathbf{m}\,\mathbf{N}\,\mathrm{d}\Omega, \quad \text{where } \mathbf{m} = \begin{bmatrix}1 & 1 & 0\end{bmatrix}^T,\\ \mathbf{S}^e_{pp} &= \int_{\Omega^e} \mathbf{N}^{\mathrm{T}}\left(\frac{1}{Q}\right)\mathbf{N}\,\mathrm{d}\Omega,\\ \mathbf{R}^e_{pp} &= \int_{\Omega^e} \mathbf{G}^{\mathrm{T}}\,\boldsymbol{\Lambda}\,\mathbf{G}\,\mathrm{d}\Omega,\\ \mathbf{F}^e_u &= -\int_{\Omega^e} \mathbf{N}^{\mathrm{T}}_u\,\mathbf{f}\,\mathrm{d}\Omega + \int_{\Gamma^{N,e}_u} \mathbf{N}^{\mathrm{T}}_u\,\bar{\boldsymbol{t}}\,\mathrm{d}\Gamma,\\ \mathbf{F}^e_p &= \int_{\Omega^e} \mathbf{N}^{\mathrm{T}} q\,\mathrm{d}\Omega - \int_{\Gamma^{N,e}_p} \mathbf{N}^{\mathrm{T}}\bar{q}\,\mathrm{d}\Gamma.\end{aligned} \tag{22}$$

Here, the operator $\mathbf{m}$ is introduced to write the hydrostatic pressure term in Voigt's notation. The integration of element matrices is carried out over the element domains using four-point Gaussian quadrature, in which the integration points are distributed inside each element to ensure accurate numerical integration.

2.2.3. FVM and FEM linear system

A unified block-partitioned form of the coupled linear system for the FVM, FEM, and their hybrid combination can be represented by grouping the corresponding sub-matrices as

$$\begin{bmatrix}\mathbf{K}_{uu} & -\mathbf{Q}_{up}\\ \mathbf{0} & \mathbf{R}_{pp}\end{bmatrix}\begin{Bmatrix}\mathbf{U}\\ \mathbf{P}\end{Bmatrix} + \begin{bmatrix}\mathbf{0} & \mathbf{0}\\ \mathbf{Q}_{pu} & \mathbf{S}_{pp}\end{bmatrix}\begin{Bmatrix}\dot{\mathbf{U}}\\ \dot{\mathbf{P}}\end{Bmatrix} = \begin{Bmatrix}\mathbf{F}_u\\ \mathbf{F}_p\end{Bmatrix}. \tag{23}$$

where vector $\mathbf{U}$ contains the degrees of freedom related to the displacements, and $\mathbf{P}$ contains the degrees of freedom related to pressure. Moreover, to solve the above system, a linear temporal discretization scheme has been employed, as the mass balance equation contains a time derivative terms. Hence, the first-order time derivatives of $\mathbf{X} = [\mathbf{U}; \mathbf{P}]$ are written as $\dot{\mathbf{X}}$, with the following time discretization

$$\begin{aligned}\dot{\mathbf{X}}_{n+\theta} &= \frac{\mathbf{X}_{n+1} - \mathbf{X}_n}{\Delta t}\\ \mathbf{X}_{n+\theta} &= \theta\mathbf{X}_{n+1} + (1-\theta)\mathbf{X}_n\end{aligned} \tag{24}$$

in which $\mathbf{X}_{n+1}$ is the vector of unknown values at the current time step $n+1$, and $\mathbf{X}_n$ is the vector of the known values at the previous time step n, and parameter θ can vary between 0 and 1, where the explicit forward Euler scheme is retrieved for $\theta = 0$, whereas the fully implicit Euler scheme has $\theta = 1$. Substituting these expressions into the discrete residual equations leads to the algebraic system corresponding to the fully implicit time discretization, obtained here by adopting $\theta = 1$

$$\underbrace{\begin{bmatrix}\boldsymbol{K}_{uu} & -\boldsymbol{Q}_{up}\\ \frac{1}{\Delta t}\boldsymbol{Q}_{pu} & \boldsymbol{R}_{pp} + \frac{1}{\Delta t}\boldsymbol{S}_{pp}\end{bmatrix}}_{\mathbf{K}}\underbrace{\begin{Bmatrix}\boldsymbol{u}^{(n+1)}\\ \boldsymbol{p}^{(n+1)}\end{Bmatrix}}_{\mathbf{X}} = \underbrace{\begin{Bmatrix}\boldsymbol{F}_u\\ \boldsymbol{F}_p + \frac{1}{\Delta t}\left(\boldsymbol{S}_{pp}\boldsymbol{p}^{(n)} + \boldsymbol{Q}_{pu}\boldsymbol{u}^{(n)}\right)\end{Bmatrix}}_{\mathbf{F}} \tag{25}$$

2.2.4. Multiscale formulation

In order to perform the multiscale analysis of the coupled HM problem, a coarse-scale computational grid is superimposed on the fine-scale mesh, on which the hydraulic and elastic properties of the medium are defined. A schematic over view of the fine-scale and multiscale grids is provided in Fig. 2. The fine-scale solution is then approximated by solving the governing equations on the coarse grid, while the detailed resolution is recovered through locally constructed basis functions.

Within this framework, the multiscale procedure consists of first restricting the fine-scale problem onto the coarse system by means of appropriate restriction operators (upscaling), and subsequently prolongating the coarse-scale solution back to the fine scale through the corresponding basis functions (downscaling).

In this work, a generalized multiscale formulation to include both FE and FV schemes is presented. To this end, a two-dimensional poromechanical system discretized with N_f fine-scale cells is considered. Therefore, the total number of unknowns is $3N_f$ (one pressure and two displacement components for each of their corresponding cells). To speed up the simulations, independent coarse grids are introduced for the deformation and flow problems, which enables flexible coarsening for each primal unknown, e.g., higher coarsening ratios for mechanics while maintaining a finer resolution for flow when required. At each time step, after applying the backward Euler scheme, the fine-scale algebraic system takes the form

$$\mathbf{K}_f \mathbf{x}_f = \mathbf{F}_f \tag{26}$$

where $\mathbf{K}_f$ is the fully implicit Jacobian matrix evaluated at time step $n+1$, $\mathbf{x}_f = \{\mathbf{u}_f, \mathbf{p}_f\}^T$ is the vector of fine-scale displacement and pressure unknowns, and $\mathbf{F}_f$ represents the source vector (contains the source contributions). Solving this system directly at full resolution is generally prohibitive for large-scale applications. To establish communication between the fine and corase scales, the multiscale approach introduces prolongation and restriction operators, which mediate the transfer of information across scales. Fine-scale quantities are projected onto the coarse space through

$$\mathbf{x}_c \approx \mathbf{R}\mathbf{x}_f, \tag{27}$$

while coarse variables are lifted back to the fine grid using

$$\mathbf{x}_f \approx \mathbf{P}\mathbf{x}_c \tag{28}$$

To enable independent coarsening of the mechanical and flow fields, both operators are constructed in block-diagonal form as

$$\mathbf{R} = \begin{bmatrix} \mathbf{R}_u & 0 \\ 0 & \mathbf{R}_p \end{bmatrix}, \qquad \mathbf{P} = \begin{bmatrix} \mathbf{P}_u & 0 \\ 0 & \mathbf{P}_p \end{bmatrix}, \tag{29}$$

where the subscripts u and p correspond to the displacement and pressure sub-block operators, respectively. This structure allows the local basis functions for flow and mechanics to be constructed independently. The restriction operator maps fine grid quantities to their coarse representation. In the finite-element formulation, this transfer follows the standard Galerkin approach and is taken as the transpose of the prolongation. In finite-volume setting, the restriction reflects the cell-averaged nature of the variables and is constructed by volume-averaging the fine grid values over each coarse control volume. The corresponding expressions are given as below

$$\begin{aligned} \mathbf{R}^{\mathrm{FE}} &= \mathbf{P}^T, \\ \mathbf{R}^{\mathrm{FV}}_{I_c(i,j),\, I_f(p,q)} &= \begin{cases} 1, & (p,q) \in \mathcal{S}_{ij}, \\ 0, & \text{otherwise}, \end{cases} \end{aligned} \tag{30}$$

where $\mathcal{S}_{ij}$ denotes the set of fine-grid indices associated with the coarse cell (i,j), and is defined as $\mathcal{S}_{ij} = \{\, (p,q) \in \Omega_f \mid \text{fine cell } (p,q) \subset \text{coarse cell } (i,j) \,\}$. By substituting the prolongation into the fine-scale equations and projecting them onto the coarse space, the global coarse-scale system for the unknowns are obtained as

$$\mathbf{K}_c \mathbf{x}_c = \mathbf{F}_c \tag{31}$$

where $\mathbf{x}_c = (\mathbf{u}_c, \mathbf{p}_c)^T$ and $\mathbf{F}_c = \mathbf{R}\mathbf{F}_f = \mathbf{R}(\mathbf{F}_u, \mathbf{F}_p)^T$ can be obtained as or equivalently,

$$(\mathbf{R}\mathbf{K}_f\mathbf{P})\mathbf{x}_c = \mathbf{R}\mathbf{F}_f \tag{32}$$

and therefore, the coarse scale unknowns follow as

$$\mathbf{x}_c = (\mathbf{R}\mathbf{K}_f\mathbf{P})^{-1}\mathbf{R}\mathbf{F}_f \tag{33}$$

and after solving the coarse system, the approximate fine-scale solution is reconstructed via

$$\mathbf{x}_f \approx \mathbf{P}\mathbf{x}_c \tag{34}$$

Fig. 3 illustrates the overall multiscale formulation for coupled hydro-mechanical problems. The diagram shows how the fine-scale and coarse-scale systems interact through the restriction and prolongation operators and the two-way transfer of displacement and pressure variables across scales, as well as the local elliptic problems and boundary constraints used to compute the basis functions for each field. These local problems provide the algebraic foundation for constructing $\mathbf{P}$ and $\mathbf{R}$ and ensure that the coarse system accurately represents the fine-scale physics.

In the block-diagonal representation of the prolongation matrix $\mathbf{P}$, the submatrices $\mathbf{P}_u$ and $\mathbf{P}_p$ are assembled from locally computed basis functions Φ as

$$\mathbf{P}_u = \left[\boldsymbol{\Phi}^u_1, \boldsymbol{\Phi}^u_2, \ldots, \boldsymbol{\Phi}^u_{N_u^H}\right], \qquad \mathbf{P}_p = \left[\Phi^p_1, \Phi^p_2, \ldots, \Phi^p_{N_p^H}\right]. \tag{35}$$

For coarse block interfaces located at the physical boundary, no-flow Neumann boundary condition is considered. No source term (i.e., non-zero flux) nor Dirichlet values are considered for those interfaces. Each basis function is obtained by solving a local

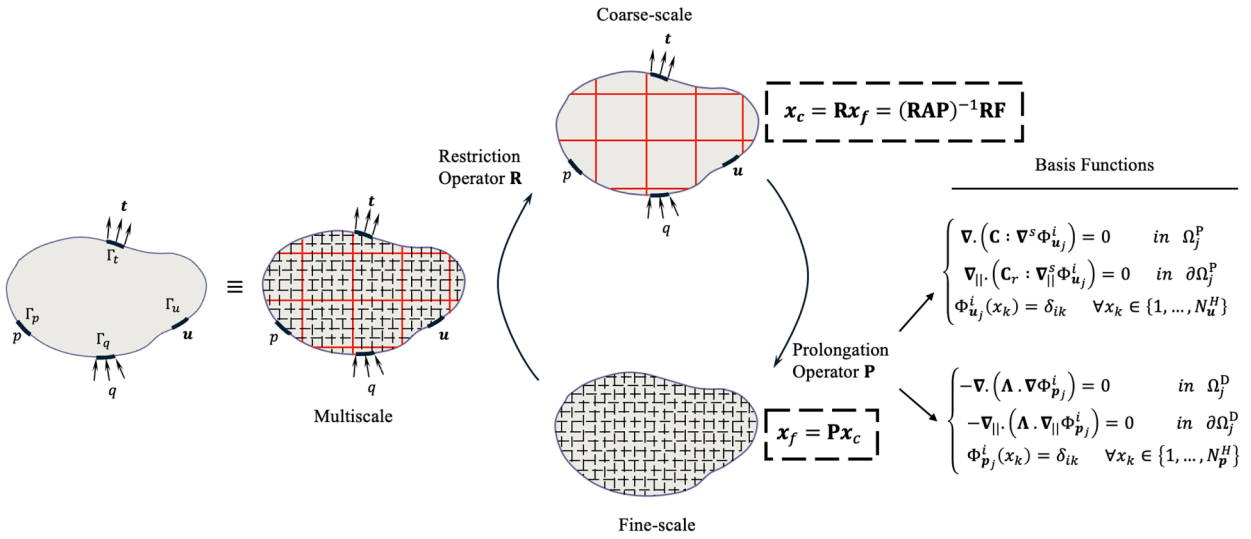

Fig. 3. Schematic description of multiscale framework of coupled hydro-mechanical problem. The illustration outlines the relationship between fine-scale and coarse-scale systems, along with the prolongation and restriction operators used to transfer variables across scales.

problem defined over a coarse block and subjected to local boundary conditions, using either FV or FE discretization depending on the fine-scale scheme employed. For the mechanical problem, the displacement basis functions $\mathbf{\Phi}_i^{u_j}$ satisfy

$$\begin{cases} \nabla \cdot (\mathbf{C} : \nabla^s \mathbf{\Phi}_i^{u_j}) = 0 & \text{in } \Omega_j^P, \\ \nabla_{||} \cdot (\mathbf{C}_r : \nabla_{||}^s \mathbf{\Phi}_i^{u_j}) = 0 & \text{on } \partial\Omega_j^P, \\ \mathbf{\Phi}_i^{u_j}(\mathbf{x}_k) = \delta_{ik}, & \forall \mathbf{x}_k \in [1, \dots, N_u^H] \end{cases} \tag{36}$$

In this context, N_u^H is the number of coarse-scale displacement nodes, where $\mathbf{\Phi}_i^{u_j}$ stands for a basis function associated with coarse displacement node i in the primal coarse block Ω_j^P, the subscript $||$ denotes a reduced problem along the primal coarse cell boundary $\partial\Omega_j^P$, and δ_{ik} is the Kronecker delta. Moreover, $\mathbf{C}_r$ denotes the reduced-dimensional elasticity tensor defined along the boundary of each coarse cell and is expressed as

$$\mathbf{C}_r^{(x)} = \begin{bmatrix} \lambda + 2\mu & 0 & 0 \\ 0 & 0 & 0 \\ 0 & 0 & \mu \end{bmatrix}, \qquad \mathbf{C}_r^{(y)} = \begin{bmatrix} 0 & 0 & 0 \\ 0 & \lambda + 2\mu & 0 \\ 0 & 0 & \mu \end{bmatrix}, \tag{37}$$

For the flow problem, the pressure basis functions $\Phi_i^{p_j}$ are obtained from

$$\begin{cases} -\nabla \cdot (\mathbf{\Lambda} \nabla \Phi_i^{p_j}) = 0 & \text{in } \Omega_j^D, \\ -\nabla_{||} \cdot (\mathbf{\Lambda} \nabla_{||} \Phi_i^{p_j}) = 0 & \text{on } \partial\Omega_j^D, \\ \Phi_i^{p_j}(\mathbf{x}_k) = \delta_{ik}, & \forall \mathbf{x}_k \in [1, \dots, N_p^H] \end{cases} \tag{38}$$

Along the coarse cell boundaries, a reduced-dimensional equilibrium equation is imposed to solve the boundary elements. Here, $\nabla_{||}$ and $\nabla_{||}^s$ denote the reduced-dimensional gradient and symmetric gradient operators acting along the boundary of each coarse block, restricted to either the x- or y-direction. The domains Ω_j^P and Ω_j^D correspond to the primal and dual coarse partitions, respectively, which define the local support regions over which the mechanical and flow basis functions are constructed. Detailed derivations of the basis functions and boundary treatments are provided in [46].

The accuracy of the multiscale approximation can be improved further through an iterative correction strategy. This procedure enables the coarse-scale solution to progressively approach the fine-scale reference within a prescribed tolerance while preserving computational efficiency.

3. Numerical results

The numerical performance of the proposed multiscale framework is assessed through a series of benchmark problems that examine the accuracy, stability, and computational efficiency of different combinations of multiscale and fine-scale finite-volume (MSFV, FS-FV) and finite-element (MSFE, FS-FE) discretizations. The tests include the Terzaghi consolidation and Mandel problem [1], followed

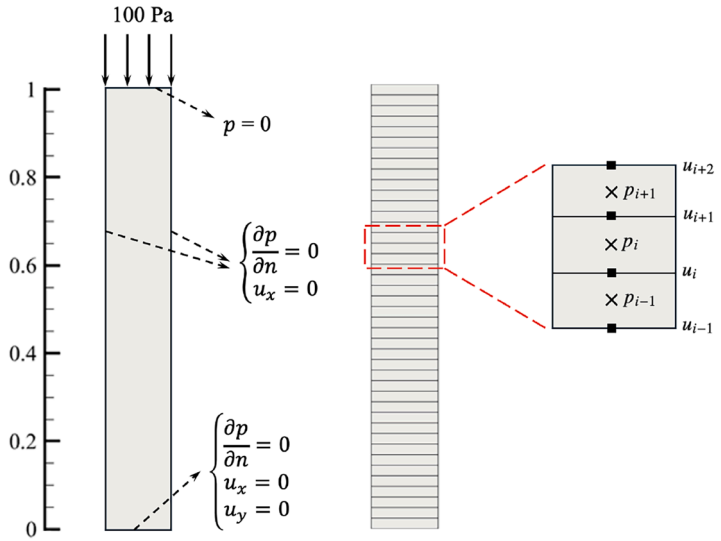

Fig. 4. Homogeneous 1D Terzaghi soil column. The figure shows the geometry, boundary conditions, and the 1×42 fine-scale mesh used for both finite-volume and finite-element discretizations.

Table 1
Material and hydraulic properties used in the Terzaghi test case.

Property	Value
Young modulus (E)	10^4 Pa
Poisson's ratio (ν)	0.2
Biot's Modulus (Q)	10^{100} Pa
Rock permeability (K)	10^{-7} m^2
Fluid viscosity (μ_f)	10^{-3} Pa · s
Biot's coefficient (α)	1

by a steady-state field-scale pressure problem with heterogeneous and anisotropic mobility distributions [50]. In all analyses, the coupled Biot system is solved in a fully implicit manner. High-resolution fine-scale (FS) simulations and analytical solutions are used as reference for validation. Throughout the manuscript, errors are computed using a scaled L_∞ norm given below. The only exception is the last example, where an L_2 error measure is used instead.

$$\epsilon = \frac{||\mathbf{x}_{ref} - \mathbf{x}||_\infty}{||\mathbf{x}_{ref}||_\infty} \tag{39}$$

where $\mathbf{x}$ denotes displacement u or pressure p. As reference, $\mathbf{x}_{ref}$ is considered from either the analytical solution or the fully resolved fine-scale simulation.

3.1. Terzaghi one-dimensional consolidation

The first verification problem corresponds to the classical one-dimensional consolidation test introduced by Terzaghi [1]. The domain, shown in Fig. 4, represents a vertical column of 0.1 m × 1 m, saturated soil subjected to a uniform compressive load of $F = 100$ Pa at the top surface, inducing pore pressure dissipation and vertical settlement over time. Drainage is allowed only at the top boundary ($p = 0$ Pa), while the bottom and lateral boundaries remain impermeable. The material properties used in the fine-grid analysis are listed in Table 1, and are taken as homogeneous and isotropic. Biot's modulus is set to a very large value to represent an incompressible pore fluid, and Biot's coefficient is taken equal to unity, which captures a fully coupled hydro-mechanical response.

The problem is solved using multiscale approach with different combinations of FE- and FV-based discretizations. The resulting MS solutions are then compared against both the fully resolved fine-scale model and the analytical solution to assess the accuracy of the developed MS-HM formulation. The simulation is performed over a duration of $t = 0.009$ s using a constant time step of $\Delta t = 0.0009$ s. For the fine-scale (FS) solution, the computational domain is discretized into 42 displacement and 42 pressure elements, providing a sufficiently accurate reference solution. The multiscale (MS) solution is constructed by applying the same coarsening ratio of 3 to both displacement and pressure unknowns. Figs. 5 and 6 present the pore pressure and vertical displacement distributions along the saturated soil column. The analytical solution is used as a reference, against which the fine-scale (FS) and multi-scale (MS) numerical results obtained with different discretization strategies are compared.

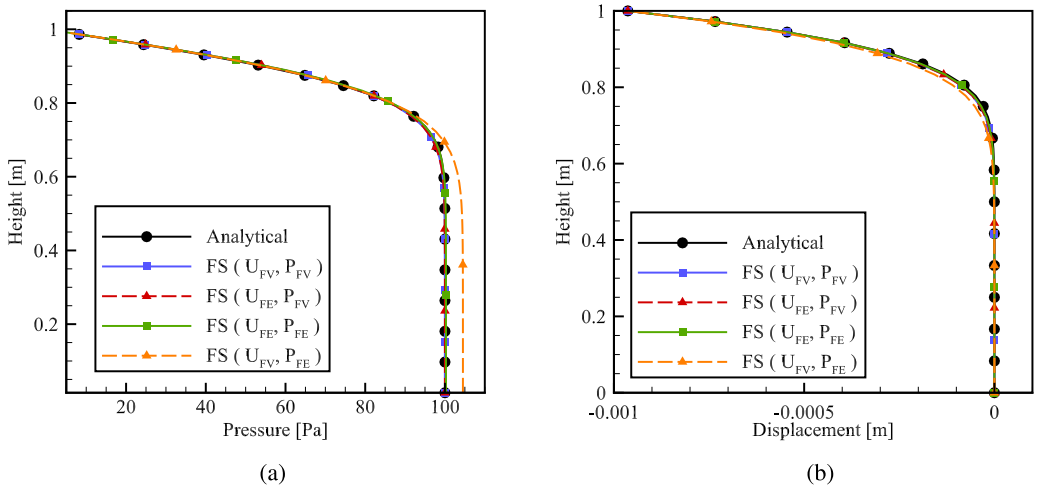

Fig. 5. A comparison of fine-scale (FS) pressure and displacement distributions along the Terzaghi soil column obtained using different finite-volume and finite-element combinations, benchmarked against the analytical solution.

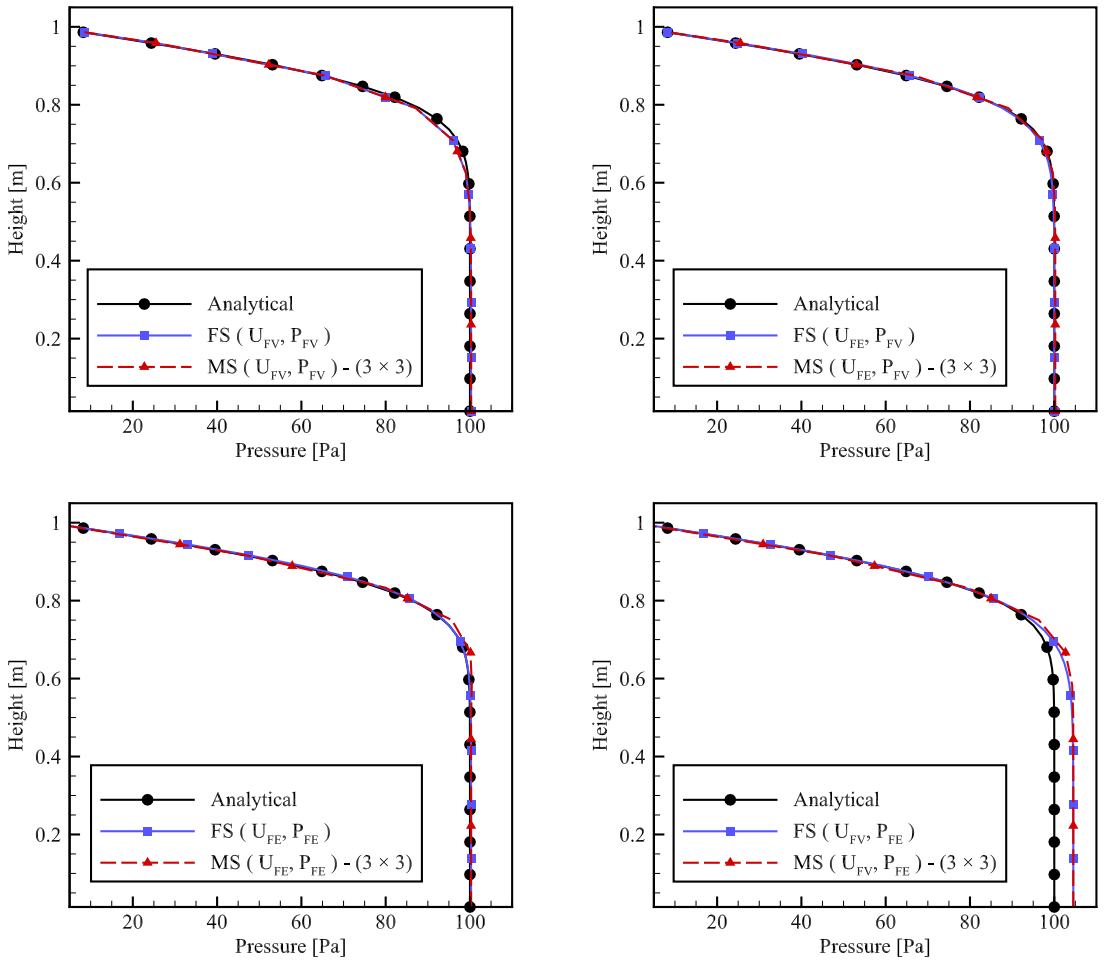

Fig. 6. A comparison of fine-scale and multiscale with 1×3 coarsening ratio for pressure distribution along Terzaghi column for different finite-volume and finite-element combinations, compared against the analytical solution.

Table 2
Terzaghi test case: accuracy of fine-scale and multiscale solutions for displacement and pressure. Here, ε_u and ε_p denote the displacement and pressure errors, respectively. The pseudo-1D fine-scale grid consists of 42 pressure and displacement elements. The multiscale error corresponds to a coarsening ratio of 3.

Method	U_{FV}, P_{FV}		U_{FE}, P_{FV}		U_{FE}, P_{FE}		U_{FV}, P_{FE}	
	ε_u	ε_p	ε_u	ε_p	ε_u	ε_p	ε_u	ε_p
MS	4.65×10^{-2}	2.21×10^{-2}	4.14×10^{-2}	1.99×10^{-2}	3.87×10^{-2}	1.96×10^{-2}	5.25×10^{-2}	4.52×10^{-2}
FS	9.7×10^{-3}	8.6×10^{-3}	9.7×10^{-3}	8.6×10^{-3}	5.9×10^{-3}	1.02×10^{-2}	3.48×10^{-2}	4.51×10^{-2}

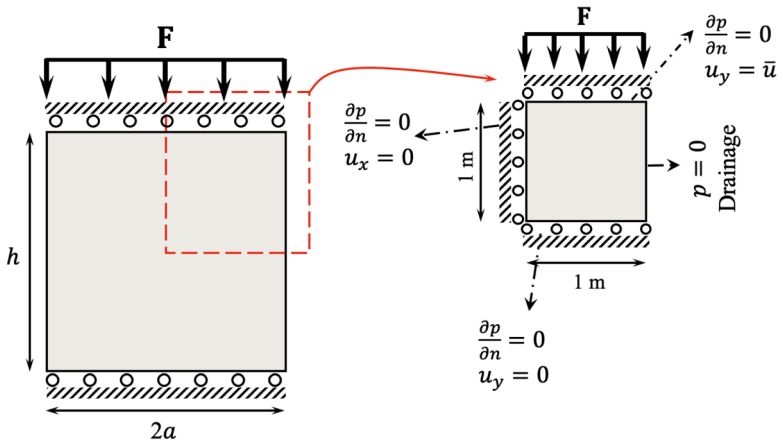

Fig. 7. Geometrical configuration and boundary conditions of Mandel's problem and the corresponding quarter symmetric model.

Both the fine-scale and multiscale solutions closely follow the analytical trends for all three discretization combinations, namely (U_{FV},P_{FV}), (U_{FE}, P_{FV}), and (U_{FE}, P_{FE}), demonstrating that the formulations remain consistent even though the MS model uses far fewer global degrees of freedom. A slight deviation appears in the pressure profile when using the (U_{FV}, P_{FE}) combination, which is mainly attributed to the coupling transfer between the staggered FV displacement field and the nodal FE pressure approximation. However, this effect becomes negligible with mesh refinement. The settlement response, however, aligns almost perfectly with the reference solution. The quality of both the multiscale and the fully resolved fine-scale solutions is evaluated separately for pressure and displacement $\mathbf{x}$ with respect to the analytical solution $\mathbf{x}_{ref}$, using the scaled L_∞-norm defines in Eq. (39).

The corresponding errors for each discretization strategy are summarized in Table 2. As expected, the fine-scale (FS) solutions generally provide the most accurate results, with errors below 1%, although the mixed combination (U_{FV}, P_{FE}) yields larger errors of approximately 3 – 4.5%. In contrast, the multiscale (MS) solutions obtained with a coarsening ratio of 3 exhibit higher error levels, typically in the range of 2 – 5%, yet remaining within a practically acceptable range.

3.2. Mandel problem

The second benchmark refers to the simulation of a two-dimensional fully coupled Mandel problem [1], in which a non-monotonic pressure behavior is observed. The problem consists of a rectangular saturated porous medium of height h and half-width a, subjected to an instantaneous uniform surface loading F at the top boundary, as depicted in Fig. 7. The lateral boundaries are drained, while the top and bottom edges are impermeable to fluid flow. The computational domain is restricted to the top-right quarter of the physical domain. Symmetry conditions are imposed along the left and bottom boundaries, the horizontal displacement is constrained on the vertical symmetry plane, $u_x = 0$, while the vertical displacement is constrained on the horizontal symmetry plane as $u_y = 0$. $\bar{u}$ is the prescribed vertical displacement resulting from the applied load on the top boundary [1]. Drainage is allowed through right boundary, and all remaining boundaries are assumed undrained, imposing $\frac{\partial p}{\partial \mathbf{n}} = 0$. The material properties used in the analysis are the same as those reported in Table 1, which results in characteristic consolidation time $t_c = 0.9$ s. The computational domain is discretized using a 45×45 uniform quadrilateral mesh for the reference fine-scale simulation. Several combinations of FE and FV schemes are examined for displacement and pressure fields, similar to the strategies considered in the Terzaghi example. For the multiscale (MS) analysis, several coarsening ratios are considered, including 3×3, 5×5, 9×9, and 15×15, whereas the time step is $\Delta t = 0.003$ s. The resulting MS solutions are then compared with both the FS and the analytical Mandel solution.

Fig. 8a shows the convergence behavior of the displacement field. The mesh is refined from 10×10 to 100×100 fine-scale cells in increments of 10, and the resulting error curve confirms that the displacement solution exhibits second-order spatial accuracy. In addition, Fig. 8b demonstrates the consistency of the time-dependent pressure solution. The error map is obtained by evaluating the pressure error at the domain center at the end of the simulation, with time steps $\Delta t \in [0.00018, 0.0018]$ s and grid size $\Delta x \in [0.01, 0.1]$ m. To identify the convergence rates, the logarithm of the error, $ln(\varepsilon_p)$, is reported. Based on the form of the numerical error,

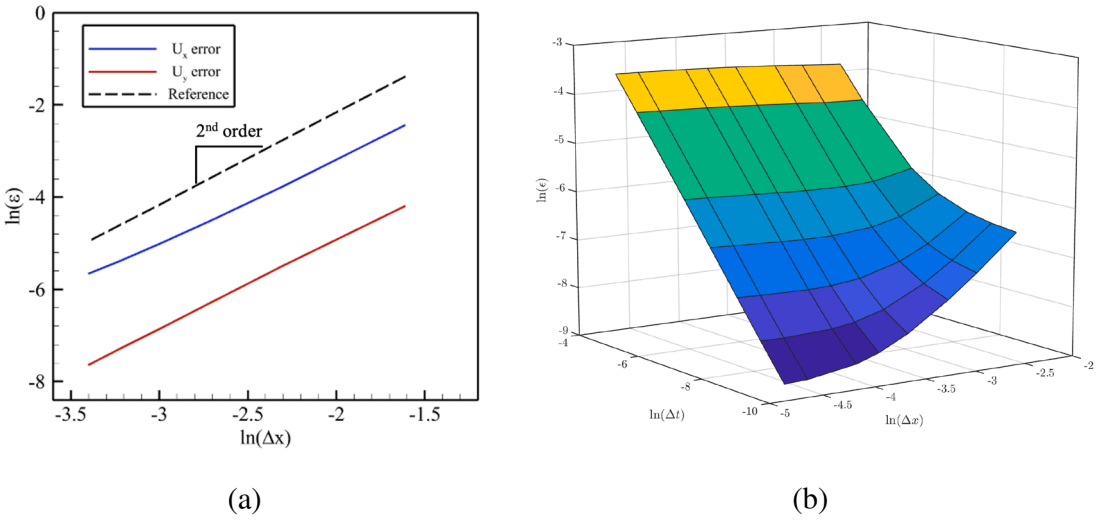

Fig. 8. (a) Spatial error plot of displacement for Mandel problem. The solution for x- and y-displacement is second-order consistent in space. (b) Logarithmic error map for the pressure field as a function of the spatial and temporal discretization sizes. The error surface clearly indicates first-order convergence with respect to time and second-order convergence with respect to space.

Table 3
Mandel test case: accuracy of the multiscale formulations for different coarsening ratios. Here, ε_u and ε_p denote the displacement and pressure errors, respectively.

Coarsening ratio	U_{FV}, P_{FV}		U_{FE}, P_{FV}		U_{FE}, P_{FE}		U_{FV}, P_{FE}	
(# of fine elems per coarse)	ε_p	ε_u	ε_p	ε_u	ε_p	ε_u	ε_p	ε_u
15×15	5.16×10^{-2}	1.78×10^{-2}	2.86×10^{-2}	6.27×10^{-3}	5.30×10^{-2}	2.04×10^{-2}	4.63×10^{-2}	1.55×10^{-2}
9×9	2.16×10^{-2}	7.08×10^{-3}	1.33×10^{-2}	1.63×10^{-3}	1.70×10^{-2}	6.95×10^{-3}	1.79×10^{-2}	2.23×10^{-3}
5×5	9.82×10^{-3}	2.96×10^{-3}	7.34×10^{-3}	1.34×10^{-3}	1.83×10^{-2}	1.38×10^{-3}	2.04×10^{-2}	5.71×10^{-3}
3×3	6.45×10^{-3}	1.80×10^{-3}	5.62×10^{-3}	1.25×10^{-3}	1.90×10^{-2}	5.80×10^{-4}	2.12×10^{-2}	6.71×10^{-3}

$\varepsilon_p = C_1\Delta t + C_2\Delta x^2$, for fixed Δx, the relation reduces to $ln(\varepsilon_p) \sim \ln(C_1) + ln(\Delta t)$, which indicates 1st order temporal accuracy. Similarly, for fixed Δt, $ln(\varepsilon_p) \sim \ln(C_2) + 2\ln(\Delta x)$, confirming 2nd order spatial accuracy. The observed slopes are consistent with the theoretical expectations for the adopted Euler integration.

Fig. 9 illustrate the temporal variation of pore pressure at the domain center, along with the pressure and displacement distributions along the central axes obtained from the fine-scale analyses. The FS results show excellent agreement with the analytical solution, including the characteristic Mandel–Cryer effect observed in the pressure history, which corresponds to the initial transient increase in pore pressure immediately after loading the pressure begins to gradually dissipate. Fig. 10 further presents the corresponding multiscale results obtained for the different coarsening ratios and discretization schemes, together with the analytical reference. The MS solutions reproduce the analytical response with high accuracy across all tested configurations, even for relatively coarse grids. As expected, increasing the coarsening ratio introduces discrepancies during the transient stage, but the overall trends and the long-term behavior remain well captured. Since this figure reports the pressure response only at the domain central point, it should be interpreted as a local comparison. A broader assessment based on the complete error analysis indicates that the (U_{FE}, P_{FV}) combination generally provides the most favorable balance between pressure and displacement accuracy, and the numerical robustness, although it is more expensive than the FV-based approach. All MS strategies converge to nearly identical results at later times.

A detailed error analysis for different multiscale discretizations and coarsening ratios is provided in Table 3. Among all tested discretization strategies, the (U_{FE}, P_{FV}) combination consistently provides the lowest error levels across all coarsening ratios. This confirms the advantage of combining the FE for displacement to preserve consistency with the variational mechanical formulation and FV for pressure to ensure numerical stability and local mass conservation.

3.3. Heterogeneous mandel problem

To assess the robustness of the proposed multiscale formulation under heterogeneous poroelastic conditions, the Mandel problem introduced in the previous section is extended to incorporate spatially varying material properties. The same domain geometry, boundary and loading conditions described earlier are retained, and only the heterogeneous material distributions and their effects on the coupled hydro-mechanical response are discussed here. In order to investigate the long-term behavior of the heterogeneous system, the simulation time is extended to $5t_c$, where t_c is the characteristic consolidation time of the corresponding homogeneous problem.

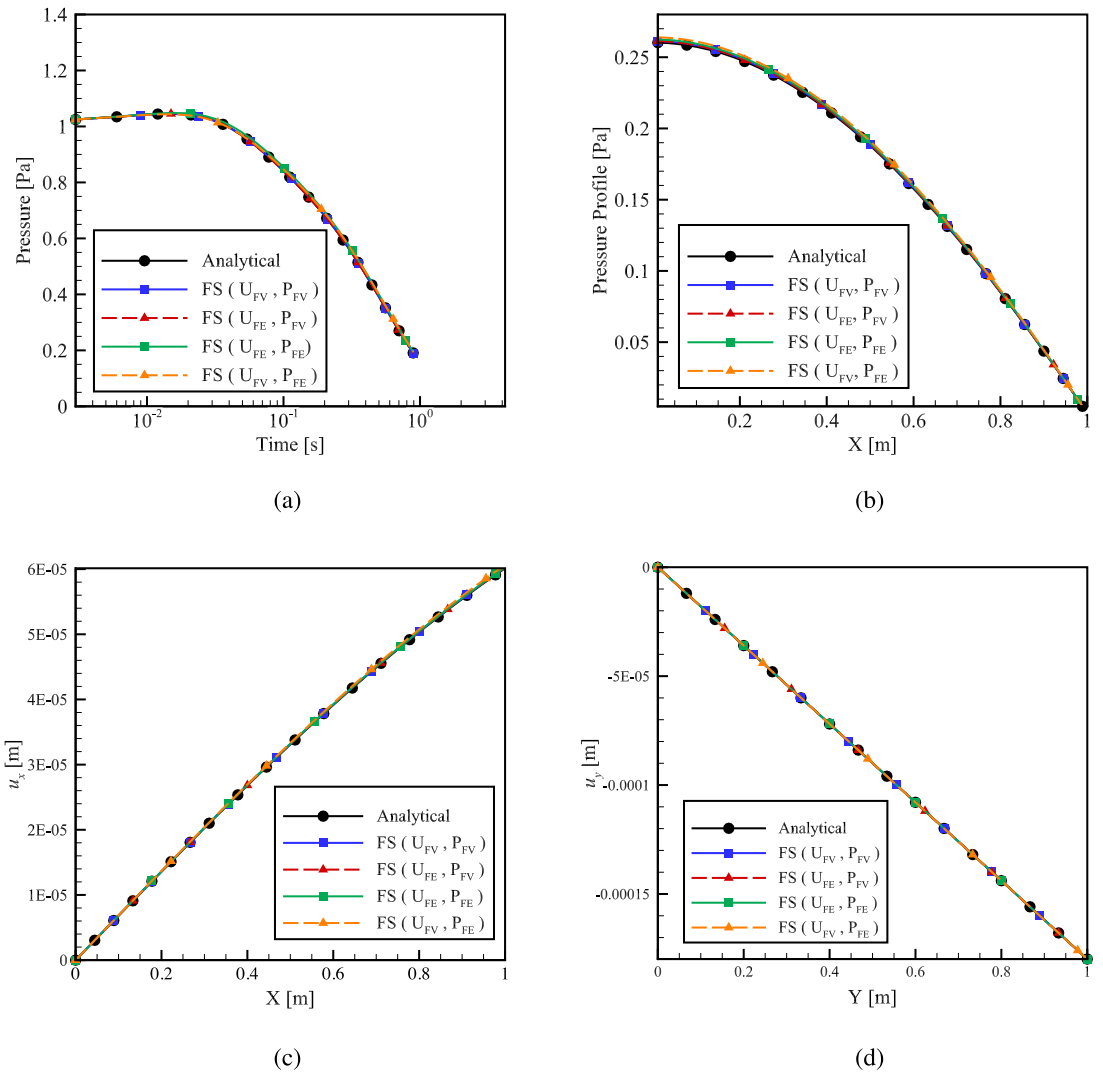

Fig. 9. A comparison of the proposed discretization combinations in fine-scale analysis with the analytical solution. The computational domain consists of a 45×45 fine grid. (a) Temporal variation of the pore pressure at the domain center; (b) pressure profile along the mid-horizontal line; (c) horizontal displacement along the mid-horizontal line; and (d) vertical displacement along the mid-vertical line.

The fine-scale reference solution is computed on a structured mesh of 45×45 elements. Two coarse-grid resolutions are examined, corresponding to coarsening ratios of 3×3 and 15×15, allowing the sensitivity of the multiscale approximation to the degree of coarsening to be evaluated.

The hydraulic mobility field Λ is modeled as a heterogeneous log-normal random field generated via Sequential Gaussian Simulation (SGS) [50]. Three anisotropic realizations are constructed by rotating the principal axis of spatial correlation at angles $\theta = 0°$, 45°, and 90° with respect to the horizontal. An additional non-directional (patchy) realization with no preferred orientation is also included. Representative distribution of $\ln(\Lambda)$ are shown in Fig. 11. For each configuration, 20 realizations are generated, and all reported results correspond to averages, which reduces realization-specific fluctuations and yields a more representative picture of the influence of heterogeneity orientation on the coupled response. The Young modulus field E is generated following the same procedure, using identical realizations and orientation angles as the mobility field. The mobility and Young's modulus fields are in the ranges of $\ln(\Lambda) \in [-14, -7]$ and $\ln(E) \in [4.4, 12.3]$, respectively, with $\nu = 0.2$ for all cases. Since both fields share the same spatial structure, only the mobility distributions are presented for brevity.

To maintain consistency with the preceding benchmarks, all four discretization combinations, $(U_{FV}, P_{FV}), (U_{FE}, P_{FV}), (U_{FE}, P_{FE})$, and (U_{FV}, P_{FE}), are examined for the case in which the Young's modulus E is homogeneous while Λ is heterogeneous. For the case in which both the E and Λ fields are heterogeneous, results are reported for the (U_{FE}, P_{FE}) combination only, since it demonstrated the smallest error among the four combinations in the homogeneous benchmarks presented earlier.

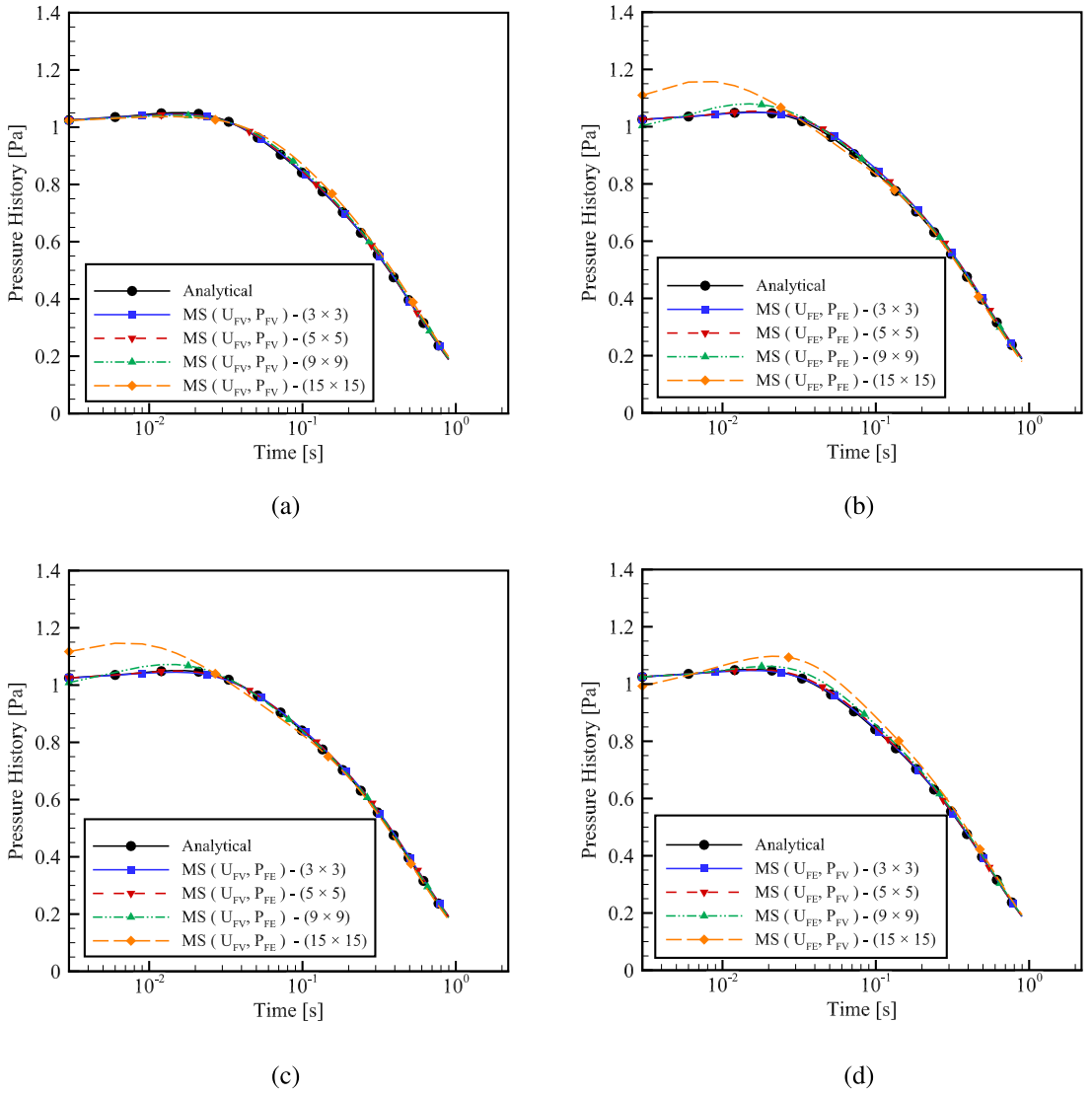

Fig. 10. The variations with time of the pressure response at the domain central point obtained by different multiscale discretization combinations for various coarsening ratios, compared against the analytical solution.

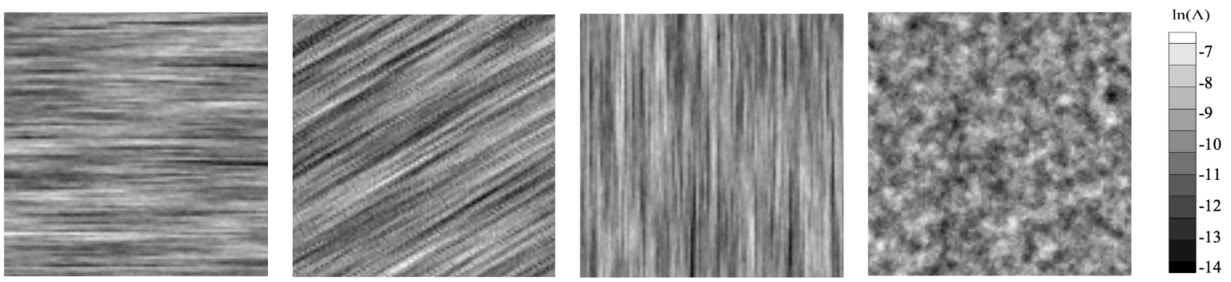

Fig. 11. Natural logarithm of the hydraulic mobility field, $\ln(\Lambda)$, for heterogeneous realizations with anisotropic structures aligned at rotation angles of $\theta = 0°$, 45°, and 90°, together with a non-directional heterogeneous distribution.

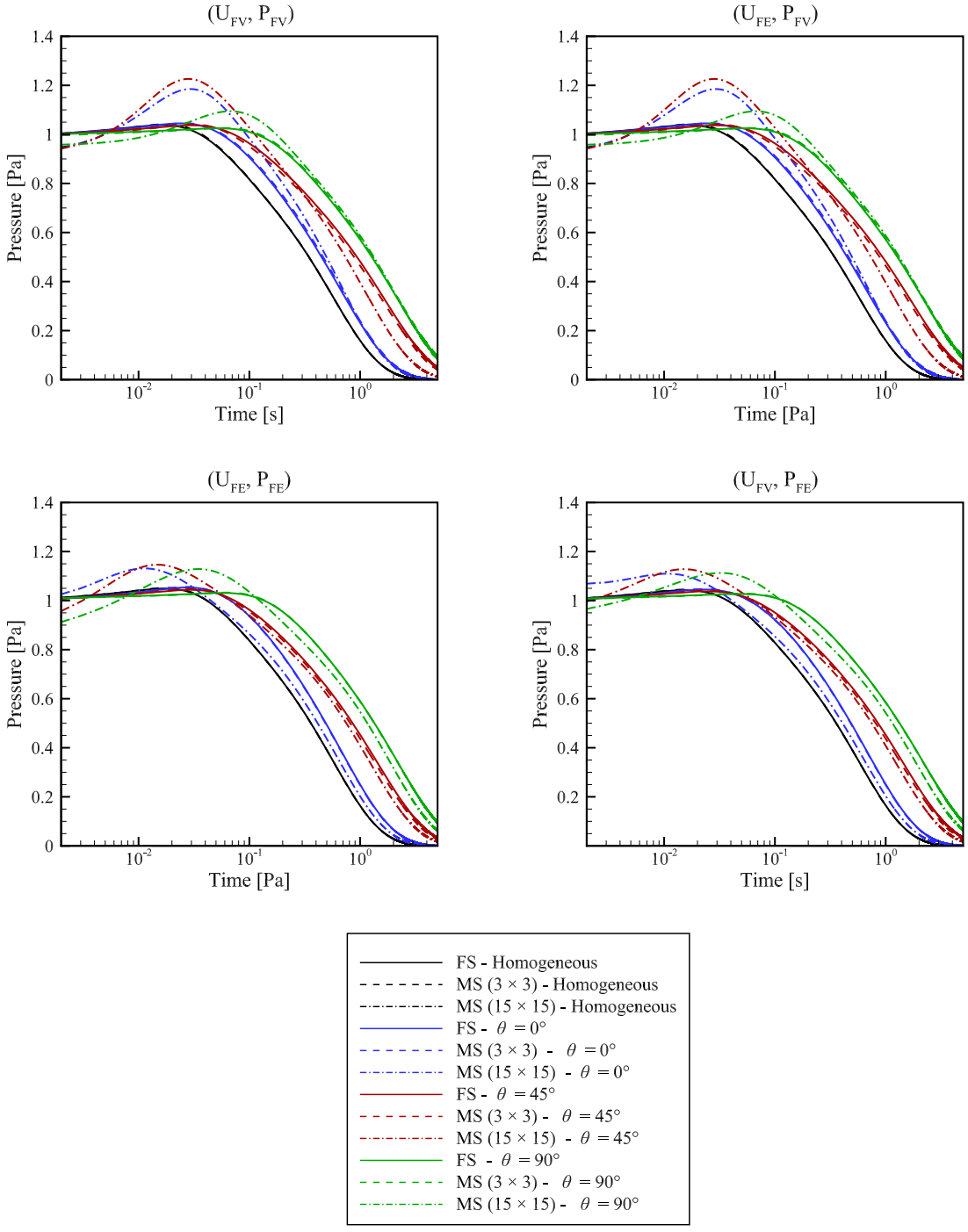

Fig. 12. Temporal evolution of pore pressure at the center of the domain for the heterogeneous Mandel problem with directionally varying mobility and uniform stiffness, obtained using the four discretization combinations. Solid lines denote the fine-scale (FS) reference solutions, while dashed and dash-dotted lines represent the multiscale (MS) solutions with $\Gamma = 3$ and 15 coarsening ratios, respectively. Note that, for the results presented in this example, the curves associated with $\Gamma = 3$ closely coincide with the corresponding FS curves.

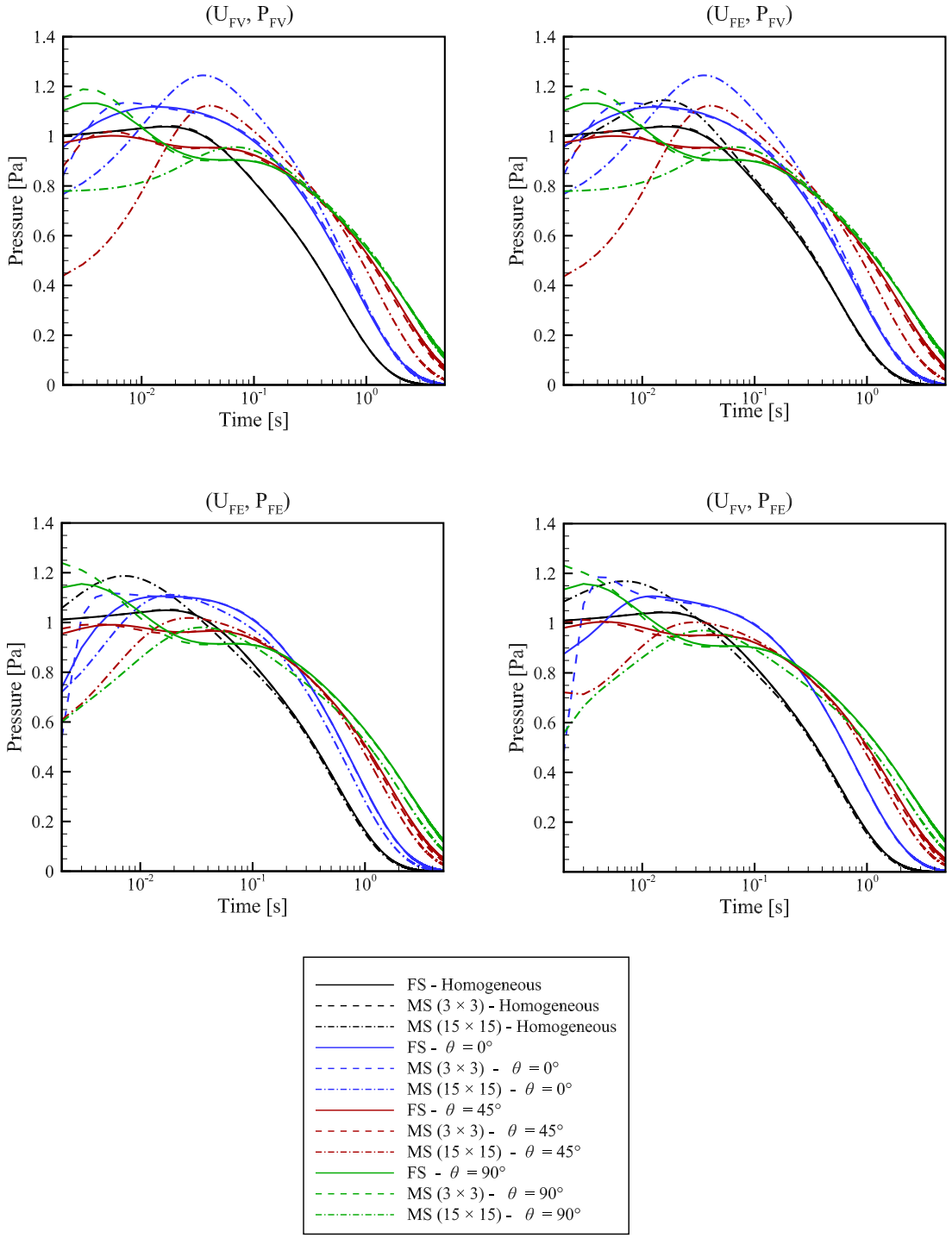

Fig. 13. Temporal evolution of pore pressure at the center of the domain for the heterogeneous Mandel problem with directionally varying mobility and Young's modulus fields, obtained using the four discretization combinations. Solid lines denote the fine-scale (FS) reference solutions, while dashed and dash-dotted lines represent the multiscale (MS) solutions with $\Gamma = 3$ and 15 coarsening ratios, respectively.

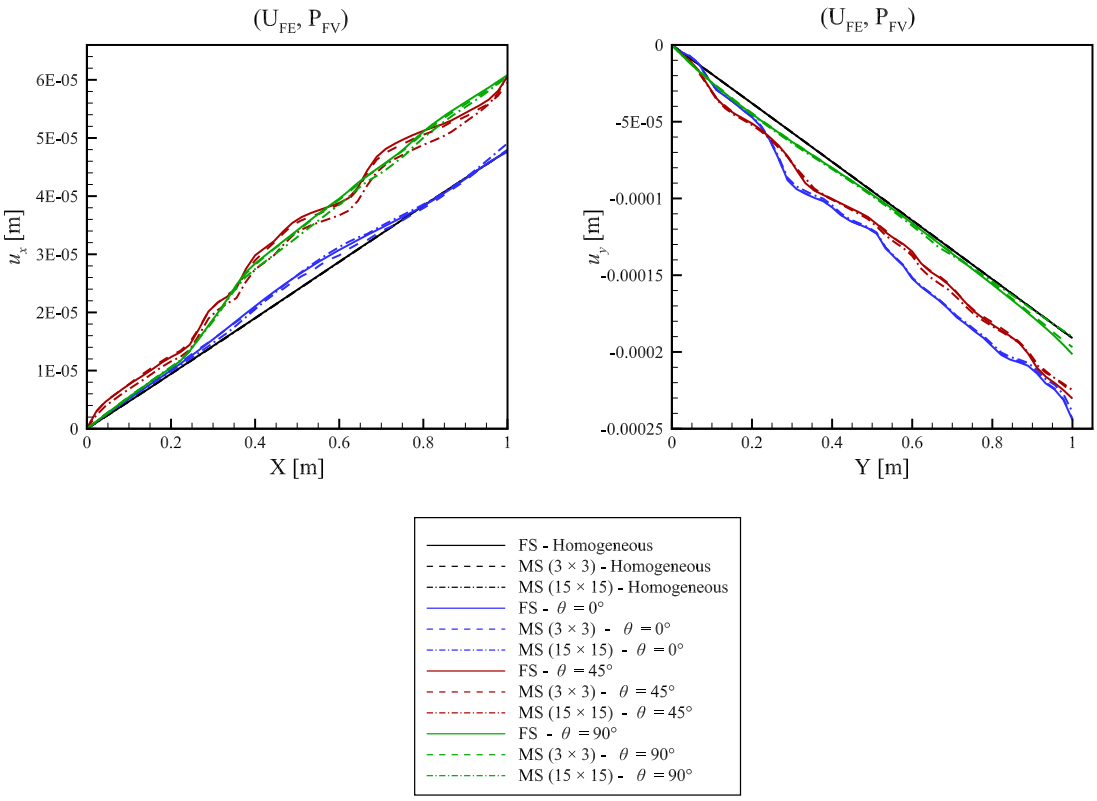

Fig. 14. Spatial distribution of the horizontal displacement u_x along $y = L_y/2$ and the vertical displacement u_y along $x = L_x/2$ for the heterogeneous Mandel problem with directionally varying mobility and young's modulus, obtained using the (U_{FE}, P_{FV}) discretization combination.

The evolution of pore pressure at the center of the domain for the case in which the Young's modulus E is homogeneous while Λ is heterogeneous, is presented in Fig. 12.

For $\theta = 0°$, high-mobility channels aligned horizontally promote rapid lateral drainage, which weakens the pressure overshoot and accelerates dissipation. At $\theta = 90°$, the dominant flow channels are oriented vertically, impeding lateral drainage. Consequently, pressure dissipation is delayed and the drainage time increases. As shown in Fig. 12. , this is manifested by a noticeable rightward shift of the pressure-history curve relative to the other orientations. Despite the pronounced influence of heterogeneity, all four combinations capture the fine-scale pressure history with good accuracy. The multiscale obtained with the 3×3 coarsening ratio closely follows the fine-scale reference throughout the entire simulation. For the 15×15 coarsening ratio, however, some discrepancies become visible during the transient stage. These deviations are most notable in cases with strong anisotropy, where the coarser basis functions are less able to resolve the sharp gradients introduced by the directional mobility field. Nevertheless, the overall dissipation trend and the long-term behavior remain well captured even at this coarser resolution, which is in line with the general behavior of multiscale methods, where a coarser grid naturally sacrifices some local resolution in exchange for a reduced computational cost.

For the combined effect of mobility and stiffness heterogeneity, the pressure histories at the center of the domain are presented in Fig. 13. When both Λ and E vary simultaneously, the pressure response becomes noticeably more complex than when only the mobility field is heterogeneous. Despite this increased complexity, all four combinations reproduce the reference solution with good accuracy, and the multiscale solutions follow the same trends with respect to coarsening ratio.

Given the superior performance of the (U_{FE}, P_{FV}) combination established in the preceding benchmarks, displacement results are reported for this pairing only.

The horizontal and vertical displacement profiles along the central axes are presented in Fig. 14. Compared to the homogeneous reference, the heterogeneous fields introduce visible local variations in both profiles. For the horizontal displacement u_x, the overall monotonic increase from the symmetry boundary toward the drained edge is preserved, but local irregularities in the gradient appear along the profile due to the spatially varying stiffness field. The slope of the u_x profile, which represents the horizontal strain $\varepsilon_x = \partial u_x/\partial x$, varies with orientation angle. Under the applied vertical load, lateral expansion is governed by the Poisson effect, $\varepsilon_x = -\nu\frac{\sigma_y}{E}$. For $\theta = 90°$, stiff channels aligned vertically offer less resistance to lateral deformation in the transverse direction, this results in larger horizontal strains compared to the homogeneous case. For $\theta = 0°$, horizontally oriented stiff zones directly oppose this lateral expansion, which produce a response closer to the homogeneous reference. For the vertical displacement u_y, the applied compressive load drives settlement along the vertical axis. For $\theta = 0°$ and 45°, the stiff zones are aligned horizontally or diagonally, which offers

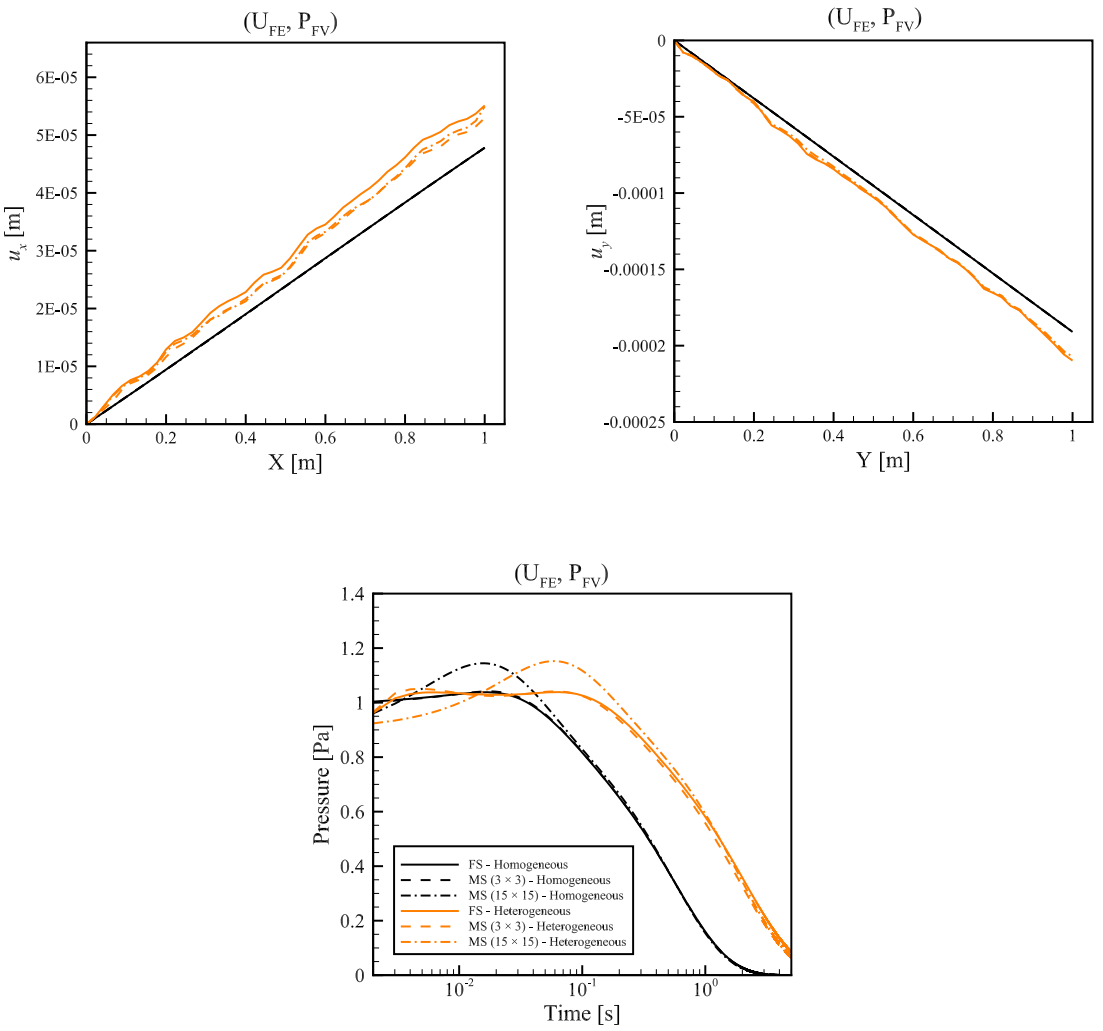

Fig. 15. Displacement profiles along the central axes and pressure history at the center of the domain for the heterogeneous Mandel problem with non-directional (patchy) mobility and stiffness heterogeneity distribution, obtained using the (U_{FE}, P_{FV}) discretization. Solid and dashed and dash-dotted lines correspond to the fine-scale reference and the multiscale approximations with $\Gamma = 3$ and $\Gamma = 15$ coarsening ratios, respectively.

relatively less resistance in the vertical loading direction and therefore produces larger settlements compared to $\theta = 90°$. Moreover, the multiscale solutions accurately capture the fine-scale behavior for both coarsening ratios.

For the non-directional heterogeneity distribution, Fig. 15, where both Λ and E vary without any preferred orientation, the pressure response exhibits a delayed dissipation compared to the homogeneous reference, reflecting the absence of preferential drainage pathways. The displacement profiles show localized fluctuations along both axes, yet the deformation trend remains consistent with the homogeneous case.

4. Computational efficiency analysis

A CPU-based performance assessment is beyond the scope of the present study. Nevertheless, to provide a meaningful estimate of the computational gains offered by the proposed multiscale strategy, an operation-based analysis [69] is carried out and discussed below. The analysis rests on the standard assumption that the cost of solving a linear system of size ζ scales as $C = \alpha\zeta^m$, where α is a constant and m is the complexity exponent of the solver. The fine-scale coupled poroelastic system involves displacement unknowns with two degrees of freedom per node (x and y direction), and pore pressure unknowns with one degree of freedom per node. For a fine-scale grid with N_f nodes, the total system size is $3N_f$, and its computational cost is estimated as

$$C_f = \alpha(3N_f)^m \tag{40}$$

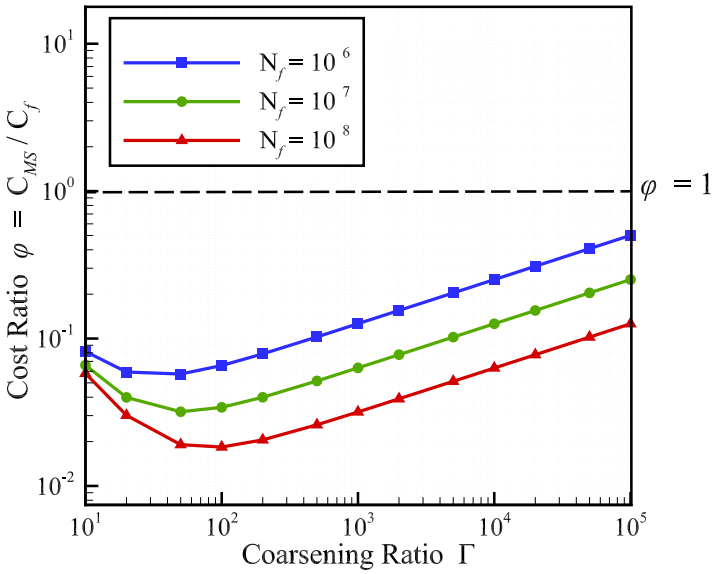

Fig. 16. Computational cost ratio, $\varphi = C_{\mathrm{MS}}/C_f$, as a function of the coarsening ratio Γ for three fine-grid resolutions ($N_f = 10^6$, 10^7, and 10^8). The horizontal line ($\varphi = 1$) denotes the break-even point, where the computational costs of the multiscale (MS) and fine-scale (FS) approaches are equal.

The proposed multiscale solver operates on a coarser grid obtained through a coarsening ratio Γ, giving a coarse-scale grid size of

$$N_c = \frac{N_f}{\Gamma} \tag{41}$$

The overall solution procedure involves two main stages: (1) construction of the multiscale basis functions, and (2) solution of the coarse-scale system. In the first stage, localized basis functions are computed for each coarse node by solving independent fine-scale subproblems. Since the coupled system carries three unknowns per fine-scale node, the cost of constructing basis functions for all N_c coarse nodes is

$$C_{basis} = 3N_c \alpha \Gamma^m \tag{42}$$

In the second stage, the coarse-scale coupled system, which involves $2N_c$ displacement and N_c pressure unknowns, is solved directly. Its cost reads

$$C_c = \alpha(3N_c)^m = \alpha(\frac{3N_f}{\Gamma})^m \tag{43}$$

The total cost of the multiscale solver is therefore

$$C_{MS} = C_{basis} + C_c = 3\alpha N_f \Gamma^{m-1} + \alpha(\frac{3N_f}{\Gamma})^m \tag{44}$$

The cost ratio φ is introduced as the ratio between the multiscale and fine-scale costs

$$\varphi = \frac{C_{MS}}{C_f} \tag{45}$$

Values of $\varphi < 1$ confirm that the multiscale solver is computationally less expensive than its fine-scale counterpart.

To evaluate φ over a range of problem sizes, three representative fine-scale grids are considered as $N_f \in \{10^6, 10^7, 10^8\}$, with coarsening ratios spanning $\Gamma \in [10, 10^5]$. Following the established practice in the literature [69], the complexity exponent is set to $m = 1.3$, which is representative of sparse linear solvers. The resulting speedup curves are shown in Fig. 16.

As seen in the figure, φ remains well below unity across all tested configurations, confirming that the multiscale approach consistently reduces computational cost relative to the fine-scale solver. Moreover, the efficiency gain becomes more pronounced as the problem size increases, which suggests that the proposed strategy is particularly well-suited for large-scale applications.

A notable feature in all curves is the presence of a well-defined minimum at an intermediate coarsening ratio, which corresponds to the optimal coarsening ratio Γ^{opt}. This minimum arises naturally from the opposing trends of the two cost contributions in Eq. (44). Setting $\frac{\partial C_{MS}}{\partial \Gamma} = 0$ yields a closed-form expression for the optimal coarsening ratio

$$\Gamma^{\mathrm{opt}} = \left(\frac{m(3N_f)^{m-1}}{3(m-1)} \right)^{\frac{1}{2m-1}} \tag{46}$$

It is worth noting that the reciprocal of φ, i.e., $1/\varphi = C_f/C_{MS}$, represents the computational speedup of the multiscale solver over its fine-scale counterpart.

5. Conclusions

A comparative investigation of multiscale finite-volume (MSFV) and multiscale finite-element (MSFE) formulations for fully coupled poroelasticity has been presented. Both methods were implemented within a unified multiscale framework based on restriction and prolongation operators that connect fine- and coarse-scale variables. The numerical results from standard benchmark tests, including Terzaghi's consolidation and Mandel poromechanics tests with homogeneous and highly heterogeneous coefficients as well as many geostatistically representative cases, demonstrated the accuracy and the robustness of the proposed approaches.

The MSFV formulation, constructed on a staggered grid, guarantees local conservation of mass and momentum and remains numerically stable even under relatively big coarsening ratios. The MSFE formulation, on the other hand, provides smooth displacement fields due to its inherent continuity of the finite-element interpolation. Among all tested configurations, the hybrid configuration of finite element for displacement and finite volume for pressure, i.e., MS (U_{FE}, P_{FV}), offers the most favorable balance between accuracy, conservation, and computational cost.

Overall, the presented results show that the proposed multiscale approach remains accurate even for poromechanical problems with complex material heterogeneity. Good agreement with the fine-scale reference solutions was obtained when both the hydraulic mobility and elastic stiffness fields were heterogeneous, including both patchy (low correlation length) and layered fields of different orientations.

Future extensions may include the three-dimensional simulations, including the thermo-hydro-mechanical coupling, and the incorporation of fracture propagation [69]. Adaptive enrichment and dynamic coarsening strategies need to be implemented to further enhance the computational efficiency of the multiscale methods, while preserving their accuracy. Furthermore, plastic deformation is required to be included in the framework especially for cyclic energy storage applications [70,71]. Finally, iterative multiscale strategies can be readily applied to improve the accuracy of the multiscale solutions [45].

CRediT authorship contribution statement

Mahsa Mehrazar: Writing – original draft, Visualization, Validation, Methodology, Conceptualization; **Cornelis Vuik:** Writing – review & editing, Supervision, Methodology, Conceptualization; **Mohammed Al Kobaisi:** Writing – review & editing, Software, Methodology, Funding acquisition; **Hadi Hajibeygi:** Writing – review & editing, Supervision, Methodology, Funding acquisition, Conceptualization.

Declaration of competing interest

The authors declare that they have no known competing financial interests or personal relationships that could have appeared to influence the work reported in this paper.

Acknowledgments

Support of the Energi Simulation Chair in Subsurface Storage and Multiscale Modeling is acknowledged.

Data availability

Data will be made available on request.

References

[1] H. Wang, Theory of Linear Poroelasticity with Applications to Geomechanics and Hydrogeology, vol. 2, Princeton university press, 2000.
[2] A.H.C. Chan, M. Pastor, B.A. Schrefler, T. Shiomi, O.C. Zienkiewicz, Computational Geomechanics: Theory and Applications, John Wiley & Sons, 2022.
[3] K. Aziz, Petroleum reservoir simulation, Applied Science Publishers, 476, 1979.
[4] K.M. Terekhov, B.T. Mallison, H.A. Tchelepi, Cell-centered nonlinear finite-volume methods for the heterogeneous anisotropic diffusion problem, J. Comput. Phys. 330 (2017) 245–267.
[5] T.J.R. Hughes, The Finite Element Method: Linear Static and Dynamic Finite Element Analysis, Courier Corporation, 2012.
[6] T. Arbogast, M.F. Wheeler, I. Yotov, Mixed finite elements for elliptic problems with tensor coefficients as cell-centered finite differences, SIAM J. Numer. Anal. 34 (2) (1997) 828–852.
[7] A. Masud, T.J.R. Hughes, A stabilized mixed finite element method for Darcy flow, Comput. Methods Appl. Mech. Eng. 191 (39-40) (2002) 4341–4370.
[8] B. Jha, R. Juanes, Coupled multiphase flow and poromechanics: a computational model of pore pressure effects on fault slip and earthquake triggering, Water Resour. Res. 50 (5) (2014) 3776–3808.
[9] N. Castelletto, M. Ferronato, G. Gambolati, Thermo-hydro-mechanical modeling of fluid geological storage by Godunov-mixed methods, Int. J. Numer. Methods Eng. 90 (8) (2012) 988–1009.
[10] J.H. Prevost, Two-way coupling in reservoir–geomechanical models: vertex-centered Galerkin geomechanical model cell-centered and vertex-centered finite volume reservoir models, Int. J. Numer. Methods Eng. 98 (8) (2014) 612–624.
[11] F.J. Gaspar, F.J. Lisbona, P.N. Vabishchevich, A finite difference analysis of Biot's consolidation model, Appl. Numer. Math. 44 (4) (2003) 487–506. ISSN 0168-9274. https://doi.org/10.1016/S0168-9274(02)00190-3
[12] F.J. Gaspar, F.J. Lisbona, P.N. Vabishchevich, Staggered grid discretizations for the quasi-static Biot's consolidation problem, Appl. Numer. Math. 56 (6) (2006) 888–898. ISSN 0168-9274. https://doi.org/10.1016/j.apnum.2005.07.002
[13] E. Ucar, E. Keilegavlen, I. Berre, J.M. Nordbotten, A finite-volume discretization for deformation of fractured media, Comput. Geosci. 22 (4) (2018) 993–1007.
[14] R. Deb, P. Jenny, Finite volume–based modeling of flow-induced shear failure along fracture manifolds, Int. J. Numer. Anal. Methods Geomech. 41 (18) (2017) 1922–1942.

[15] D.A. Di Pietro, R. Eymard, S. Lemaire, R. Masson, Hybrid finite volume discretization of linear elasticity models on general meshes, in: Finite Volumes for Complex Applications VI Problems & Perspectives: FVCA 6, International Symposium, Prague, June 6–10, 2011, Springer, 2011, pp. 331–339.
[16] E. Keilegavlen, J.M. Nordbotten, Finite volume methods for elasticity with weak symmetry, Int. J. Numer. Methods Eng. 112 (8) (2017) 939–962.
[17] J.M. Nordbotten, Cell-centered finite volume discretizations for deformable porous media, Int. J. Numer. Methods Eng. 100 (6) (2014) 399–418.
[18] J.M. Nordbotten, Stable cell-centered finite volume discretization for Biot equations, SIAM J. Numer. Anal. 54 (2) (2016) 942–968.
[19] R. Deb, P. Jenny, Modeling of shear failure in fractured reservoirs with a porous matrix, Comput. Geosci. 21 (5) (2017) 1119–1134.
[20] P. Jenny, S.H. Lee, H.A. Tchelepi, Adaptive fully implicit multi-scale finite-volume method for multi-phase flow and transport in heterogeneous porous media, J. Comput. Phys. 217 (2) (2006) 627–641.
[21] M.G.D. Geers, V. Kouznetsova, W.A.M. Brekelmans, Multi-scale computational homogenization: trends and challenges, J. Comput. Appl. Math. 234 (7) (2010) 2175–2182, ISSN 0377-0427. https://doi.org/10.1016/j.cam.2009.08.077
[22] M.G.D. Geers, V.G. Kouznetsova, K. Matouš, J. Yvonnet, Homogenization methods and multiscale modeling: nonlinear problems, Encycl. Comput. Mech. Second Ed. (2017) 1–34. https://doi.org/10.1002/9781119176817.ecm2107
[23] R. Helmig, J. Niessner, B. Flemisch, M. Wolff, J. Fritz, EfficientModeling of flow and transport in porous media using multiphysics and multiscale approaches, in: Handbook of Geomathematics, Springer, 2010, pp. 417–457.
[24] P. Jenny, S.H. Lee, H.A. Tchelepi, Multi-scale finite-volume method for elliptic problems in subsurface flow simulation, J. Comput. Phys. 187 (1) (2003) 47–67.
[25] Y. Wang, H. Hajibeygi, H. Tchelepi, Algebraic multiscale linear solver for heterogeneous elliptic problems, in: ECMOR XIII-13th European Conference on the Mathematics of Oil Recovery, European Association of Geoscientists & Engineers, 2012, pp. cp–307.
[26] O. Møyner, K.-A. Lie, A multiscale restriction-smoothed basis method for high contrast porous media represented on unstructured grids, J. Comput. Phys. 304 (2016) 46–71.
[27] L.A. Caudillo-Mata, E. Haber, C. Schwarzbach, An oversampling technique for the multiscale finite volume method to simulate electromagnetic responses in the frequency domain, Comput. Geosci. 21 (5) (2017) 963–980.
[28] R.D. Cook, Modeling for Stress Analysis, New York: Wiley, 1994.
[29] O.C. Zienkiewicz, R.L. Taylor, The Finite Element Method for Solid and Structural Mechanics, Elsevier, 2005.
[30] T.Y. Hou, X.-H. Wu, A multiscale finite element method for elliptic problems in composite materials and porous media, J. Comput. Phys. 134 (1) (1997) 169–189.
[31] Y. Efendiev, V. Ginting, T.Y. Hou, Multiscale finite element methods for nonlinear problems and their applications, Commun. Math. Sci. 2 (4) (2004) 553–589.
[32] Y. Efendiev, V. Ginting, T. Hou, R. Ewing, Accurate multiscale finite element methods for two-phase flow simulations, J. Comput. Phys. 220 (1) (2006) 155–174.
[33] Y. Wang, H. Hajibeygi, H.A. Tchelepi, Monotone multiscale finite volume method, Comput. Geosci. 20 (3) (2016) 509–524.
[34] M. Schneider, B. Flemisch, R. Helmig, K. Terekhov, H. Tchelepi, Monotone nonlinear finite-volume method for challenging grids, Comput. Geosci. 22 (2) (2018) 565–586.
[35] Y. Efendiev, T.Y. Hou, Multiscale Finite Element Methods: Theory and Applications, Springer Science & Business Media, vol. 4, 2009.
[36] M. Vasilyeva, E.T. Chung, Y. Efendiev, J. Kim, Constrained energy minimization based upscaling for coupled flow and mechanics, J. Comput. Phys. 376 (2019) 660–674.
[37] F. Furtado, V. Ginting, F. Pereira, M. Presho, Operator splitting multiscale finite volume element method for two-phase flow with capillary pressure, Transp. Porous Media 90 (3) (2011) 927–947.
[38] A. Kozlova, Z. Li, J.R. Natvig, S. Watanabe, Y. Zhou, K. Bratvedt, S.H. Lee, A real-field multiscale black-oil reservoir simulator, SPE J. 21 (06) (2016) 2049–2061.
[39] S. Shah, O. Møyner, M. Tene, K.-A. Lie, H. Hajibeygi, The multiscale restriction smoothed basis method for fractured porous media (F-MsRSB), J. Comput. Phys. 318 (2016) 36–57.
[40] R.J. de Moraes, J.R.P. Rodrigues, H. Hajibeygi, J.D. Jansen, Multiscale gradient computation for flow in heterogeneous porous media, J. Comput. Phys. 336 (2017) 644–663.
[41] M. Cusini, A.A. Lukyanov, J. Natvig, H. Hajibeygi, Constrained pressure residual multiscale (CPR-MS) method for fully implicit simulation of multiphase flow in porous media, J. Comput. Phys. 299 (2015) 472–486.
[42] M. Cusini, C. van Kruijsdijk, H. Hajibeygi, Algebraic dynamic multilevel (ADM) method for fully implicit simulations of multiphase flow in porous media, J. Comput. Phys. 314 (2016) 60–79.
[43] M. HosseiniMehr, M. Cusini, C. Vuik, H. Hajibeygi, Algebraic dynamic multilevel method for embedded discrete fracture model (F-ADM), J. Comput. Phys. 373 (2018) 324–345.
[44] N. Castelletto, H. Hajibeygi, H.A. Tchelepi, Hybrid multiscale formulation for coupled flow and geomechanics, in: ECMOR XV-15th European Conference on the Mathematics of Oil Recovery, European Association of Geoscientists & Engineers, 2016, pp. cp–494.
[45] N. Castelletto, S. Klevtsov, H. Hajibeygi, H.A. Tchelepi, Multiscale two-stage solver for Biot's poroelasticity equations in subsurface media, Comput. Geosci. 23 (2) (2019) 207–224.
[46] N. Castelletto, H. Hajibeygi, H.A. Tchelepi, Multiscale finite-element method for linear elastic geomechanics, J. Comput. Phys. 331 (2017) 337–356.
[47] H. Zhou, H.A. Tchelepi, Two-stage algebraic multiscale linear solver for highly heterogeneous reservoir models, in: SPE Reservoir Simulation Conference, SPE, 2011, pp. SPE–141473.
[48] M. Ţene, M.S. Al Kobaisi, H. Hajibeygi, Algebraic multiscale method for flow in heterogeneous porous media with embedded discrete fractures (F-AMS), J. Comput. Phys. 321 (2016) 819–845.
[49] T.T. Garipov, M. Karimi-Fard, H.A. Tchelepi, Discrete fracture model for coupled flow and geomechanics, Comput. Geosci. 20 (1) (2016) 149–160.
[50] H. Hajibeygi, G. Bonfigli, M.A. Hesse, P. Jenny, Iterative multiscale finite-volume method, J. Comput. Phys. 227 (19) (2008) 8604–8621.
[51] S. Dana, M.F. Wheeler, Convergence analysis of fixed stress split iterative scheme for anisotropic poroelasticity with tensor Biot parameter, Comput. Geosci. 22 (5) (2018) 1219–1230.
[52] M. Borregales, F.A. Radu, K. Kumar, J.M. Nordbotten, Robust iterative schemes for non-linear poromechanics, Comput. Geosci. 22 (4) (2018) 1021–1038.
[53] J. Kim, H.A. Tchelepi, R. Juanes, Stability and convergence of sequential methods for coupled flow and geomechanics: fixed-stress and fixed-strain splits, Comput. Methods Appl. Mech. Eng. 200 (13–16) (2011) 1591–1606.
[54] N. Castelletto, J.A. White, H.A. Tchelepi, Accuracy and convergence properties of the fixed-stress iterative solution of two-way coupled poromechanics, Int. J. Numer. Anal. Methods Geomech. 39 (14) (2015) 1593–1618.
[55] S. Klevtsov, N. Castelletto, J.A. White, H.A. Tchelepi, Block-preconditioned Krylov methods for coupled multiphase reservoir flow and geomechanics, in: ECMOR XV-15th European Conference on the Mathematics of Oil Recovery, European Association of Geoscientists & Engineers, 2016, pp. cp–494.
[56] J.H. Adler, F.J. Gaspar, X. Hu, C. Rodrigo, L.T. Zikatanov, Robust block preconditioners for Biot's model, in: International Conference on Domain Decomposition Methods, Springer, 2017, pp. 3–16.
[57] L. Bergamaschi, Á. Martínez, RMCP: relaxed mixed constraint preconditioners for saddle point linear systems arising in geomechanics, Comput. Methods Appl. Mech. Eng. 221 (2012) 54–62.
[58] J.A. White, R.I. Borja, Block-preconditioned Newton–Krylov solvers for fully coupled flow and geomechanics, Comput. Geosci. 15 (4) (2011) 647–659.
[59] J.A. White, N. Castelletto, H.A. Tchelepi, Block-partitioned solvers for coupled poromechanics: a unified framework, Comput. Methods Appl. Mech. Eng. 303 (2016) 55–74.
[60] C. Janna, M. Ferronato, G. Gambolati, A block FSAI-ILU parallel preconditioner for symmetric positive definite linear systems, SIAM J. Sci. Comput. 32 (5) (2010) 2468–2484. https://doi.org/10.1137/090779760
[61] M. Ferronato, Preconditioning for sparse linear systems at the dawn of the 21st century: history, current developments, and future perspectives, Int. Sch. Res. Not. 2012 (1) (2012) 127647. https://doi.org/10.5402/2012/127647
[62] F.J. Gaspar, F.J. Lisbona, C.W. Oosterlee, R. Wienands, A systematic comparison of coupled and distributive smoothing in multigrid for the poroelasticity system, Numer. Linear Algebra Appl. 11 (2-3) (2004) 93–113.

[63] F.J. Gaspar, C. Rodrigo, On the fixed-stress split scheme as smoother in multigrid methods for coupling flow and geomechanics, Comput. Methods Appl. Mech. Eng. 326 (2017) 526–540.
[64] P. Luo, C. Rodrigo, F.J. Gaspar, C.W. Oosterlee, Multigrid method for nonlinear poroelasticity equations, Comput. Vis. Sci. 17 (5) (2015) 255–265.
[65] R.W. Lewis, B.A. Schrefler, The Finite Element Method in the Static and Dynamic Deformation and Consolidation of Porous Media, John Wiley & Sons, 1999.
[66] M.A. Murad, A.F.D. Loula, On stability and convergence of finite element approximations of Biot's consolidation problem, Int. J. Numer. Methods Eng. 37 (4) (1994) 645–667.
[67] C. Rodrigo, F.J. Gaspar, X. Hu, L.T. Zikatanov, Stability and monotonicity for some discretizations of the Biot's consolidation model, Comput. Methods Appl. Mech. Eng. 298 (2016) 183–204.
[68] I. Sokolova, M.G. Bastisya, H. Hajibeygi, Multiscale finite volume method for finite-volume-based simulation of poroelasticity, J. Comput. Phys. 379 (2019) 309–324.
[69] F. Xu, H. Hajibeygi, L. Sluys, Multiscale extended finite element method for deformable fractured porous media, J. Comput. Phys. 436 (2021) 110287. https://doi.org/10.1016/j.jcp.2021.110287
[70] K. Ramesh Kumar, H. Hajibeygi, Multiscale simulation of inelastic creep deformation for geological rocks, J. Comput. Phys. 440 (2021) 110439. ISSN 0021-9991, https://doi.org/10.1016/j.jcp.2021.110439
[71] K. Ramesh Kumar, H. Honorio, D. Chandra, M. Lesueur, H. Hajibeygi, Comprehensive review of geomechanics of underground hydrogen storage in depleted reservoirs and salt caverns, J. Energy Storage 73 (2023) 108912. ISSN 2352-152X, https://doi.org/10.1016/j.est.2023.108912